2

GCA-TR-73-4-N

DEFINITION RESEARCH STUDY

F. F. Marmo and J. Pressman

(NASA-CR-133836) DEFINITION RESEARCH STUDY Final Report (GCA Corp.) 82 p HC $6.25 CSCL 22B

N73-30843

Unclas

G3/31 15219

GCA CORPORATION

Bedford, Massachusetts

FINAL REPORT

Contract No. NASW-2395

Prepared for

NATIONAL AERONAUTICS AND SPACE ADMINISTRATION

HEADQUARTERS

Washington, D. C.

April 1973

GCA-TR-73-4-N

DEFINITION RESEARCH STUDY

F.F. Marmo and J. Pressman

by

GCA CORPORATION
GCA TECHNOLOGY DIVISION
Bedford, Massachusetts

FINAL REPORT

Contract No. NASW-2395

Prepared for

NATIONAL AERONAUTICS AND SPACE ADMINISTRATION
HEADQUARTERS
Washington, D.C.

April 1973

I

TABLE OF CONTENTS

Section	Title	Page
1.0	INTRODUCTION	1
2.0	SURVEY OF SPACECRAFT OPTICAL POLLUTION	2
3.0	BEHAVIOR OF RELEASED MATERIAL	13
4.0	EXPERIMENTAL PROGRAM	47
5.0	FUTURE WORK	66
	APPENDIX A	67
	APPENDIX B	69
	REFERENCES	77

Table		
2.1	LIST OF SOME SPACECRAFT CONTAMINATION OBSERVATIONS	6
3.1	COMPARISON OF VARIOUS MECHANISMS FOR ACCELERATING DEBRIS PARTICLES OF UNIT RADIUS AND DENSITY AWAY FROM A SPACECRAFT	15
3.2	CALCULATION FOR VARIOUS ALTITUDES AND SIZE PARTICLES	21
3.3	CALCULATION OF M_s AND N_s USING EQUATION 3.12 FOR CONTINUOUS RELEASE	22
3.4A	CALCULATION OF M_s FOR SUDDEN IMPULSIVE RELEASE OF Δ m MASS AS A FUNCTION OF TIME (sec)	23
3.4B	SAME AS TABLE 4A EXCEPT CALCULATION	24
3.5	THEORETICAL VALUES	28
3.6	CALCULATIONS OF BRIGHTNESS	31
3.7	CALCULATION OF INTEGRATED MASS AND INTEGRATED NUMBER OF MOLECULES FOR EFFLUENT GASES AT STEADY RATE $\dot{m}$	44
4.1	SPACE LIFETIMES FOR VARIOUS POSSIBLE PARENT COMPOUNDS	60
4.2		62

TABLE OF CONTENTS (continued)

Figure		Page
3.1	COORDINATES FOR A PARTICLE P IN THE DEBRIS COMET SURROUNDING A SPACECRAFT OF NOMINAL RADIUS R_s.	17
3.2	GEOMETRY FOR CALCULATION OF THE RADIANCE OF SUNLIT DEBRIS NEAR A SPACECRAFT.	26
3.3	MEAN FEEE PATHS VS. ALTITUDE.	34
3.4	PRESSURE AND DENSITY PRODUCED BY OUTGASSING VS. DISTANCE FROM THE SPACECRAFT SURFACE	38
3.5	DENSITY, PRESSURE, AND FLUX AT THE SPACECRAFT SURFACE, PRODUCED BY OUTGASSED MOLECULES RETURNING TO THE SPACECRAFT, VS. ALTITUDE	40
3.6	DENSITY, PRESSURE, AND FLUX RATIOS AT THE SPACECRAFT SURFACE, PRODUCED BY OUTGASSED MOLECULES RETURNING TO THE SATELLITE	41
4.1	ECCENTRIC MODE LASER/RECEIVER CONFIGURATION	52
4.2	SUGGESTED OPTICAL CONFIGURATION TO ACCOMODATE THE SKEWED BEAM AND RELATED IMAGING SYSTEM GEOMETRY	54

1.0 INTRODUCTION

This is the Final Report of work prepared under NASA contract No. NASw-2395. The required tasks involve the investigation of the physical behavior and characteristics of the ensembles of plasma gas and/or dust as it relates to the self contamination of manned orbiting vehicles. The research study is applicable to the Space Shuttle, space rendezvous, and Command Service Module orbiting flights. One of the initial tasks involved the compilation of an updated survey on the present state of knowledge in the scientific areas of interest to this project, the results of which are presented in Section 2 of this report. A major task in the present investigation involved the definition of a systematic experimental program designed to yield the required empirical data associated with the plasma, neutral gas, and/or the particulate matter surrounding the orbiting vehicles associated with the Shuttle Missions. The required theoretical analyses have been completed to acquire a better understanding of the behavior of materials to be released from the orbiting and/or sub-satellite shuttle vehicles. The results of these analyses which are presented in Section 3 have been employed to define some general experimental design recommendations directly applicable to the Space Shuttle Program requirement. An initial experiment for measuring the dynamic behavior, inventory, and physical characteristics of particulates in the space craft vicinity is described in Section 4. The technique employs an on-board laser which is capable of high sensitivity and can monitor preselected target areas during any phase of a given orbit. An appropriately designed on-board laser probe has various applications to the earths atmospheric studies related to the sensitive detection and measurement of the inventory and distribution of earth minor constituents and/or pollutants.

An additional application to the determination of photo-dissociation rates of cometary species is also presented in Section 4. Finally an integrated experiment is suggested and discussed in Section 5 in greater detail.

2.0 SURVEY OF SPACECRAFT OPTICAL POLLUTION

2.1 INTRODUCTION

The results of a detailed study and an extension of work performed originally under NASA Contract # NASW-1745 is presented herein. This former effort involved both a detailed investigation of gaseous and particulate cloud contamination environments in the vicinity of a manned spacecraft as well as the applicability of the overall contamination cloud technologies and results to various extant problems of cometary physics.

The specific manned spacecraft of interest herein involves the orbital stage of the space shuttle which is characterized generally by the capability of transporting selected personnel, general cargo, and specific scientific payloads between the surface of the earth and relatively low altitude terrestrial orbits. This shuttle system can accomodate a wide variety of configurations including orbital characteristics, scientific and applications payloads, and diverse engineering activities at costs which appear both reasonable and competitive. For example, space shuttle has been viewed as the future analog to such aircraft platforms as the NASA Convair 990 aircraft inasmuch as men and equipment will be transported to earth orbital station whereupon the indicated experiment or measurement will be performed, following which the payload will be returned to earth without sacrifice of the intrinsic flight hardware. This operational mode can clearly both accommodate a relatively high flight rate owing to the reuseable nature of the space shuttle stages as well as the participation of individual investigators for on-station performance of specific experiments where warranted. As a result, the space shuttle system which should be operational in the final years of the current decade will provide new dimensions for the performance of both space research and continuing applications measurements which will be timely, flexible, and financially competitive. Several features of this experimental capability and flexibility intrinsic to the space shuttle configuration are listed below:

1. Payloads up to 15 feet in diameter and 60 feet in length can be accommodated by the Orbiter.

2. Mission duration from lift-off to landing of at least seven days of self-sustaining lifetime are provided in the Orbiter for four men. Trade-offs for longer duration missions involve additional expendables against payload weight.

3. An internal, sealable tunnel with a standard interface provides for shirtsleeve access between the crew compartment and payloads.

4. The Orbiter has the capability to deploy a payload on-orbit, including placing and abandoning, or docking a payload to a stabilized third body.

5. The Orbiter has the capability of docking to stabilized modules with subsequent retrieval, handling, and stowage for orbit transfer or return to earth. The docking/deployment mechanism is standardized for all payloads.

6. Airlock, hatch, handholds, line attach points, etc., are provided for EVA operations.

7. The Orbiter has the capability for deploying and releasing up to seven payloads in orbit.

8. The Orbiter has the capability of retrieving and stowing up to three payloads in orbit and returning them to earth.

9. Provisions are made for TV monitoring of critical functions prior to payload deployment and release.

The design, performance, and assessment of several proposed experimental investigations utilizing the space shuttle orbital platform require detailed knowledge of the content, behavior, and interaction of the contaminant cloud in the near environment of the spacecraft. As a consequence, the overall problem of spacecraft contamination represents the major topic of interest in the present program.

Unfortunately, only sparse data are available currently concerning the problem of the spacecraft associated contaminant cloud, although several specific experiments are scheduled to be performed under the Skylab Program in the near future to define and measure

both possible contamination sources in manned spacecraft as well as their overall effects on specific experimental programs.

The specific experiments on Skylab dedicated to measurement of the associated contaminant cloud include T025, a contamination coronagraph experiment designed to measure light scattered by small particles (adjacent to and removed from the spacecraft) for relatively small solar elongation angles. In a second experiment, T027, a photometer will make similar measurements for larger elongation angles at over several wavelengths. This latter experiment T027 also has a sample array to provide data on accumulated total contaminants over a variety of surfaces as well as a sensitive quartz-crystal microbalance to detect real-time depositions of less than a few micrograms/cm^2. Indirect evidence of contamination may also be obtained from anomalous behavior of other Sky-Lab experiments.

The fact that such contaminant clouds indeed exist was derived from the results obtained in the Gemini and Apollo programs. In addition, the reported results of the Soviet space flight program indicate the presence of relatively large particles in their associated spacecraft contamination clouds. Specifically in this regard, the results of the Gemini X and Gemini XII micrometeoroid experiments indicate that a tenuous contaminant atmosphere accompanied the spacecraft. Furthermore, this conclusion was verified by the ground-based analysis of an optical array located externally on Gemini XII which demonstrated decreased transmission in the ultraviolet spectral region of the optical glasses owing to the contaminant deposition. In addition, direct evidence of contamination has been obtained in several cases of measured depositions on the Gemini and Apollo windows. Finally, in the cases of short-lived or very low altitude orbiting vehicles there may also exist contaminations associated with either the passages through or the proximity to the ambient earth's atmosphere.

In general, contamination debris can interfere with the performance of specific scientific experiments by such effects as direct

condensation of material on exposed optical surfaces, scattering and emission of radiation, and diverse effects from the gaseous contaminants. Several sources of this latter gaseous material probably include the spacecraft atmosphere, propellant operation, purging of the batteries of fuel cells, etc. A more detailed discussion of the problems involved in both the generation and subsequent characteristic behavior of the contaminant cloud is available in Reference 1 in which specific critical problems relative to the general spacecraft contamination problems were investigated.

2.2 EVIDENCE FOR CONTAMINANT ATMOSPHERE SURROUNDING SPACECRAFT

At present substantial evidence has been accumulated which indicates that a gaseous and particulate environment surround the spacecraft, albeit it is not certain what the detailed consequences may be of such an accompanying environment to specific operational modes of the spacecraft. Consequently, for the purpose of this report it does not seem warranted to engage in a discisive examination of the various phenomena reported. Rather, reference (1) is made to Table 2.1 which lists and describes briefly the observed contamination effects. No attempt is made at being exhaustive and some observations may have been omitted.

The important aspect of the observations to date is that for the most part they are descriptive and perhaps even anecdotal possessing more of the nature of happenstances rather than deliberate, carefully programmed experiments to examine the problem. Consequently, major uncertainties remain to a large extent unresolved, such as the chemical nature of the contaminants, fractionation between gas and particles, space and time behavior, charged or uncharged, etc.

The observations of contamination in general fall into two main classifications:

a. External atmospheric effects resulting from rocket firings, dumps, (urine, water, etc.), surface desorption or cabin leakage which create an increase in the background brightness around the spacecraft.

TABLE 2.1

LIST OF SOME SPACECRAFT CONTAMINATION OBERVATIONS

		Reference
Mercury	Observation of "space fireflys" by John Glenn.	2
Mercury & Gemini	Inability of astronauts to see stars fainter than second magnitude.	2
Gemini	Window contamination observed from inside spacecraft and during EVA.	3
Voskhod 1	Cosmonauts Komarow, et al saw glowing particles.	4
Gemini 12	Deposition of material on optical samples flown by Martin Co. during engine exhaust and staging events.	4
Gemini 10 and 12	Surface analysis of micrometeroid delectors flown by Hemenway and Hallgren.	4
Pegasus II	Film on spacecraft observed curved trajectories of particles around ship.	5
OGO III	Even after 6 months operation mass spectrometer read three orders of magnitude higher gas density than predicted from satellite drag.	5
Apollo 15 Lunar Orbit	Mass spectrometer produced spectra of unexpected complex variety indicating spacecraft emission.	6

b. Surface deposition effects from the above operations which may effect sensitive optical surface, thermal coatings, etc. Of particular interest is the Apollo 15 lunar orbit mass spectrometer observation which mandated, by virtue of the long term persistence of the contamination, the conclusion that the associated contaminant cloud was composed of droplets and not gas.

2.3 CONTAMINANT SOURCES

It is difficult to identify exactly the potential sources of contaminants other than for a specific type of spacecraft. Such sources arise from exposed spacecraft materials which desorb or outgas and from materials emitted to external space by virtue of leakage or intentional discharge. Outgasing from surface materials depends on their respective exposed areas in various directions, their desorptive properties, and the thermal history of the surface. Direct emission may result from fuel-cell purging, reaction control system (RCS) engine firings, waste disposal, and direct spacecraft leaks. Waste disposal may include condensate dumps, molecular sieve dumps, waste tank/fecal dryer dumps, and waste tank/biocide dumps.

It is neither feasible under this program nor does it represent its function to analyze in detail the potential contamination of the space shuttle whose design configuration even regarding its major design aspects are still not established. Rather as part of the total design of experiments for determining self-contamination there will be described some of the available information on the ATM-Skylab configuration self-contamination problem. It is noted that pending the actual operation of this ATM-Skylab with its self-contamination experiments, the data from ground tests and theory are not completely satisfactory even for this well established configuration.

A fundamental question regards the size of the crystals created by water vapor or liquid emitted into space [7] since if they are sub-micron, e.g., circa 0.1 micron, they will display significantly reduced cross section values for visible radiation, whereas if they are

larger than one micron their respective cross-section will be relatively higher since they will appear as Mie scatterers.

It should be noted that a significant program exists to minimize or eliminate contamination sources in spacecraft. For example, materials selected for space usage must pass the test of several criteria on thermal and outgassing properties; nevertheless, contamination is to a large extent unavoidable and will require careful in situ characterization through specific experiments.

A rough guide to the degree and nature of contamination which may occur on the Space Shuttle is presented in Appendix A (extracted from Reference 8) which represents estimated data for the Apollo Spacecraft. It is recognized that such data serve only as a guide and basis of new calculations for the Shuttle. In addition, the results of the Ball Brothers study[9] is of particular value in assessing the sources of contamination.

2.4 MATHEMATICS - PHYSICAL MODELS OF SPACECRAFT CONTAMINATION

The basic point presented in this brief review of various models of the contamination cloud associated with spacecraft is that to-date there have been no direct measurements of such contamination of such a nature as to provide an adequate check on theoretical estimates or models. Theoretical models are necessary in order to understand the nature of the contamination problem, to generalize from one type of spacecraft to another under somewhat different conditions and to "make a fix" on contamination sources.

Ney and Huch,[2] performed an early analysis of surface brightness of spacecraft corona as a function of the mass spectrum rate of particulate matter. In passing, it is noted that their Figure 2 should be labeled as 2 lbs/hr rather than 2 lbs/min. They employed simple drag deceleration to remove particles from the vicinity of the spacecraft. For particle size greater than 1 micron, they note that the surface brightness depends only on dm and not on size. Newkirk[8] prepared the classic work on spacecraft contamination examining the

dyanmics of particulate material ejected from spacecraft and concluded that the residence time of particles for orbits in the lower atmosphere is controlled by aerodynamic drag and by radiative pressure at higher altitudes. Calculations of radiance were performed for a variety of conditions and the derived results suggested that the optical environment may at times be so unfavorable as to preclude observations of faint sources such as solar corona, zodiacal light gegenschein, etc.

The results of another extensive study[9] (dealing also with contaminant source) concluded that molecular scattering effects were small but that particulate scattering from water emanating from the Command Service Module represented a major problem. An evaluation was also made of the probability of contaminant condensation on critical optical elements which was considered the most serious threat.

The General Electric group[3,13] reported photometric observation and theory which set a low limit (30 times less) than Newkirk's evaluation of the radiance due to particulate scattering. Buffalano[7] calculated that the formation of large crystals should not occur in cabin leaks, that scattering from leaked cabin atmosphere would be small and that attention was best paid to other contaminant causes. Kovar[4] reviewed the problem and calculated that the particulate cloud for the assumed model would be brighter than zodiacal light but recommended the necessity of experimental measurements in view of the uncertainties. Silicone coating of optical surfaces was also considered a strong possibility.

Grenda et al,[5] observed curved contaminant particle trajectories in the vicinity of a spacecraft and concluded that electrostatic forces were operative and should be determined experimentally in situ. Kovar, et al[14] calculated the brightness of the debris cloud surrounding manned spacecraft and concluded that day-light observations of dim-light sources will probably not be feasible from Apollo and ATM unlike Newkirk who felt the situation for Apollo to be at worst marginal. A fog of silicones surrounding the ATM and condensing on optical surfaces was also of concern to Kovar, et al.

Buffalano[15] conceptualized a theoretical model of the Apollo oxygen releases. He found the scatterers to be particles of size 100-1000μm, subliming, and of e-folding time, t_s, approximately 100 minutes.

Sharma and Buffalano[16] studied the temperature and size histories of liquid H_2, O_2, and H_2O and concluded that micron size liquid drops tend to freeze quickly. At 640 km, the calculated e-folding time was 15(H_2), 120(O_2), and 1100(H_2O) sec. At distances greater than 10 earth radii these times increase by about an order of magnitude.

Pressman[1] performed an initial survey of the contaminant concentration around spacecraft, found the reduced free-path effect, and derived a graphical technique for addressing the scattering problem.

Scialdone,[17,18] in the most systematic attempt to date, useful for design criteria, derived equations for concentrations and fluxes of contaminants around a spacecraft. He also made an analytical connection with space vacuum chamber simulation of this problem. A gap in Scialdone's treatment is that he assumes arbitrarily that scattered particles have their velocities diminished by a half and moreover he avoids the problem of angular scattering by again assuming arbitrarily that angular scattering out of the volume is matched by angular scattering into the volume.

The differences between various investigators such as Newkirk and Kovar et al remain. They are dependent upon such unknown parameters as particulate size distribution, refractive index, and mass efflux and basic differences in theoretical approach. The problem area is one that is insistent on carefully designed experiments for further resolution.

As a matter of convenience for rapid calculations and internal completeness, the important governing formulae and related graphs taken from Scialdone[17] for the molecular drag case are presented in Section 3. It is noted that for the higher and cis-lunar orbits radiation pressure dominates and here the considerations of Newkirk[8] are still valid. In Figure 3.5, the rapid falloff of returning flux,

φ'' can be seen from 200-1000 km and the relative flattening our beyond this altitude. It is noted that these purely theoretical and highly simplified relationships have as yet not been subjected to specific verification in the space environment.

2.5 SPACE-CHAMBER SIMULATION

A brief point is made concerning the usefulness of space-chamber simulation of self-contamination. This involves the connection that can be made between self-contamination in a vacuum chamber and in space. Experiments designed to be flown for the purpose of measuring self-contamination can be calibrated and validated in these apparata which have been designed to provide a simulated operational environment to measure possible Skylab (at present) contamination plumes and particle impingement. Such chambers can provide quantitative data on gas mass flow and characteristics, particle size and velocity distribution, charged nature of effluents, surface contamination effects and plane effects during steady state or discrete event operational modes.

Of particular interest are the results of Scialdone[17] who concluded that space simulation chambers can provide returning fluxes and self-contamination comparable to those occurring in space up to an altitude of about 400 km. For higher altitudes he states the self-contamination will be greater. However, in this case, ground results can be related to those obtained in space, provided either that the wall captive coefficient is known or the ratio of returned to emitted flux at the spacecraft surface is measured. Mention is also made of the study of Wallace and Chuan[19] of self-contamination in a space chamber.

Some remarks follow on ground simulation programs although this subject will not be pursued to a comprehensive extent because of its tangential nature to the main purpose of our program.

A major current chamber program is the Skylab Contamination Ground Test Program being conducted by Martin Marietta (MMC) which

has been designed to provide a simulated operational environment to measure expected contamination plumes and particle impingement effects.

Mention is made (with no attempt at completeness) of the work on space chamber simulation of contamination. Of interest is the work of Klingman[20] on measurement of sticking coefficients and their theoretical calculation by Monte Carlo technique. Tashbar,[21] has used the Chamber-A vacuum facility to test the chamber contamination problem and is planning to test ultraviolet effects in formation of polymerized contamination film. Kurtz and Williams[22] have developed a holographic camera and are measuring particle size distributions and particle velocity vectors for actual Skylab contamination sources. Greyerbiehl[23] has devised a system for measuring directly chamber solar simulation intensity data. Surface desorption which is a sensitive function of solar input may thus be more carefully determined. Dewey[24] has developed a complex computerized infrared simulation system for thermal vacuum ground testing of spacecraft. This system can simultaneously follow as many as 30 separate time-varying intensity profiles for irradiation of different areas of a test spacecraft. Such a procedure more closely simulates real conditions and should be useful in the contaminant study problem. Reference is also made to Visentine et al[25] for a report on the preparation and control of a large chamber for contamination sensitive tests.

Finally, mention should be made of the Space Molecular Sink Simulation designed by Stephens and Wallace[26] to minimize self-contamination by employing cryogenic walls composed of small angle wedges.

Consequently, it is concluded that a variety of chambers are available for validating and calibrating space contamination measurement experiments. Despite the utility of such chambers, because of the limitation on extremely low self-contamination coefficients and on close duplication of spacecraft operational modes, it is considered essential to perform contamination experiments and measurements in space.

3.0 BEHAVIOR OF RELEASED MATERIAL

In this section the theoretical aspects of the released material behavior is discussed in order to analyze more specifically any desired controlled release experiments as indicated in the previous discussion. Specifically, two experiments, involving both a gaseous and a particulate release, are designed to elucidate the dynamics of the interaction of released gases and particulates in the environs of the spacecraft, to provide a check on previously developed theory, and to provide the observational base for a more sophisticated and realistic theory. A third experiment is designed to take unique advantage of the space environment to obtain basic molecular and spectroscopic data for general scientific and specific cometary purposes.

Consequently, the theoretical models which are presently available and suitable for calculation purposes will be presented first. The deficiencies of these models will be detailed. Second, specific calculations will be made over a range of parameters to assist in the experimental design, e.g., release rate, concentration, integrated column amount, optical thickness, etc. These calculations will then be utilized for specific experimental design recommendations.

It should be noted that none of the theories upon which the design calculations are based have as yet been subjected to any specific experimental test. Consequently, it is felt that while the present theories are certainly not adequate they can be utilized for initial experimental design. Thus, it is expected that the theory may be revised on the basis of the performance of the recommended experiments.

3.1 Theory of and Calculations of Released Particle Behavior

3.1.1 Theoretical Background

An analysis of the deficiencies of particle behavior theory is presented below as well as a succinct summary of this theory and specific parameterized calculations suitable for experimental design.

3.1.1.1 Deficiencies

The current theory of particle behavior surrounding a satellite is due to Newkirk[8]. It is an approximate theory deficient in several respects. First, it does not analyze the shape of the released particulate matter cloud but only obtains a parameter which is considered representative of the total size of the accompanying cloud. Second, this representative parameter, R_M is obtained by estimating the distance at which the velocity of the particles relative to the satellite (for forward emitted particles) is decelerated to zero. No substantial analysis is made of the non-collinear scattering. Actually, the concentrations predicted represent an under-estimate since the decelerated particles will start moving back in a returning flux to the satellite somewhat similar to the Scialdone[18] theory for effused molecules. Consequently, an adequate theory of requisite detail is not currently available.

3.1.1.2 Existing Theory

Drag Force - First, the drag forces are considered since existing theory is based upon a simple decelerating resisting medium. The dominant mechanisms for accelerating debris particles away from the spacecraft are aerodynamic drag and solar radiation pressure as shown in Table 3.1. Other mechanisms such as Poynting-Robertson drag, Coulomb drag, Lorentz force, and convective drag are smaller and may be neglected.[1] The treatment below is summarized from Newkirk.[8]

Aerodynamic drag - The spacecraft is assumed to have the velocity, v through a resisting medium and the particles in the present case are ejected with velocity, u_o parallel to v. Since the orbital velocity, v (for satellites) in general is much greater than u_o, then

$$\frac{4}{3}\pi r^3 \rho \dot{u} = \rho_a v^2 \pi r^2 \tag{3.1}$$

or

$$\dot{u} = \frac{3\rho_a v^2}{4\rho r} \tag{3.2}$$

At 160 km, $\dot{u} = \frac{4.2 \times 10^{-1}}{\rho}$ for unit radius.

TABLE 3.1

COMPARISON OF VARIOUS MECHANISMS FOR ACCELERATING DEBRIS PARTICLES OF UNIT RADIUS AND DENSITY AWAY FROM A SPACECRAFT

Mechanism (1)	Representative satellite (2)	h(km) (3)	ρ_a(g/cm^3) (4)	ν(cm/sec) (5)	μ(cm sec^{-2}) (unit radius) (6)
Aerodynamic drag	Close-in Gemini	160	10^{-12}	7.5×10^5	4.2×10^{-1}
	Close-in Apollo	320	4×10^{-14}	7.4×10^5	1.7×10^{-2}
Solar radiation pressure	Synchronous Cis-lunar	4×10^4	–	3×10^{10}	3.4×10^{-5}
Solar wind	Cis-lunar	$\sim9\times10^4$	10^{-23}	5×10^7	2×10^{-8}

Taken from Ref. (8)

This force, as will be seen later, is the major force affecting particles emitted from low altitude satellites. The decleration is inversely proportional to particle size as can be seen from Equation (3.2).

Radiation Pressure - The simple first order equation presented below is followed by brief mention of some of the complexities of radiation pressure. The deceleration is considered, in the geometrical optics approximation, to be due to radiation pressure as given by:

$$P_R = \pi r^2 \frac{F_o}{c} \tag{3.3}$$

where F_o = flux of sunlight on the particle and c = velocity of light.

Then

$$\frac{4}{3} \pi r^3 \rho \dot{u} = \frac{\pi r^2 F_o}{c} \tag{3.4}$$

and

$$\dot{u} = \frac{3}{4} \frac{F_o}{\rho c r} \tag{3.5}$$

for a particle of radius, r and density, ρ. Again here the acceleration increases as the size of the particle decreases as can be seen from Equation (3.5).

Actually the calculation related to radiation pressure is quite difficult to perform in the general case (where the particle may be of the approximate size or smaller than the wavelength) since the effective cross section and the vector direction of the acceleration depend in a complex fashion on the surface slope, orientation, and index of refraction of the dust particles as well as on the polarization and frequency distribution of the incident radiation.

A more extensive discussion of the general case is presented in Reference 1.

Model - Except for the Lorentz force, all the mechanisms: aerodynamic drag, radiation pressure, charge drag, and solar wind pressure have the mathematical characteristics of motion through a resisting medium. Thus, the acceleration of particles away from the spacecraft can be made in rather general terms. In the satellite

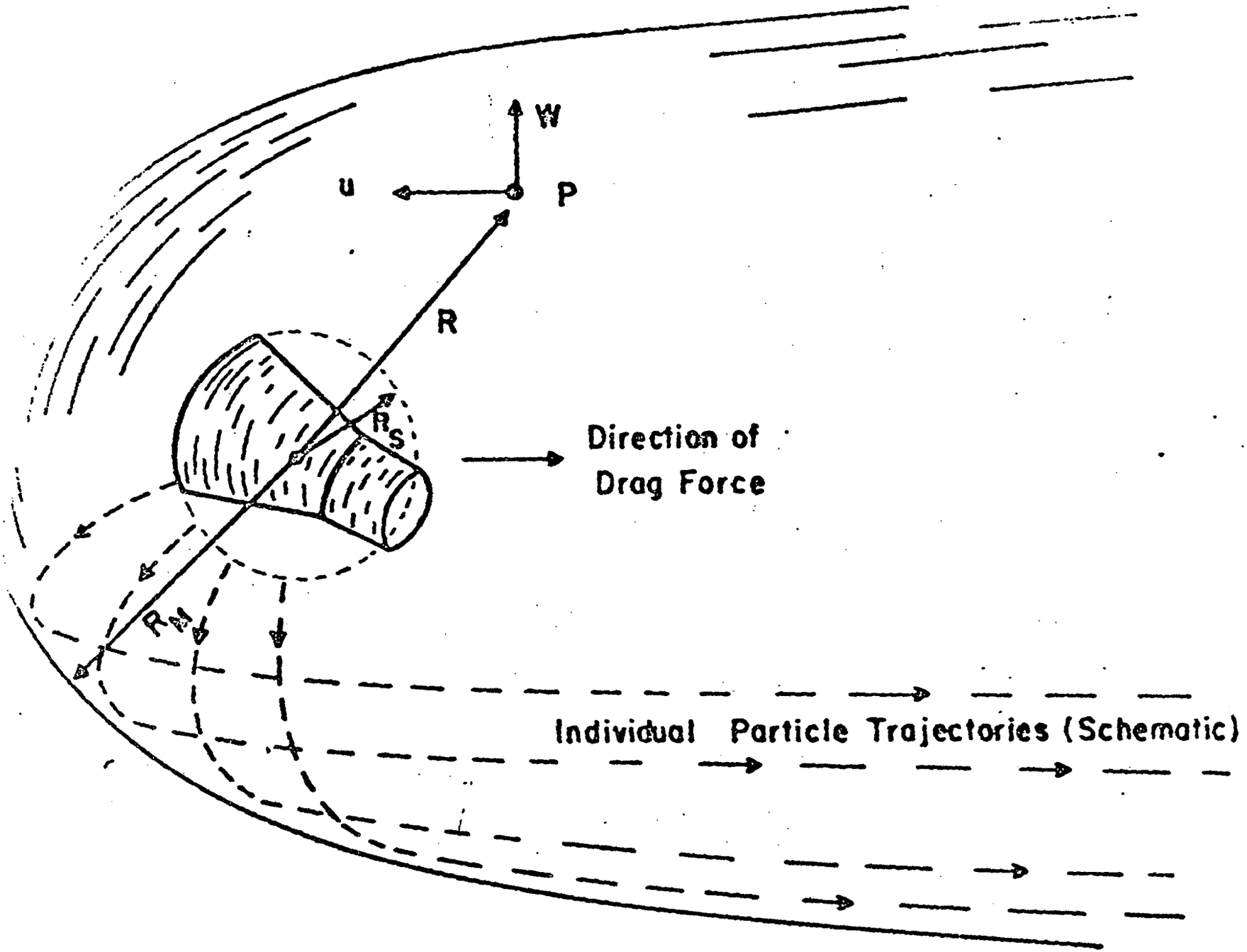

Figure 3.1 Coordinates for a particle P in the debris comet surrounding a spacecraft of nominal radius R_s. Taken from Ref. 1.

reference frame, an ejected spherical particle of radius r is considered to have velocity components, u directed against the drag direction and w perpendicular to the drag direction (Figure 3.1).

Continuous ejection has the following parametric description. In the first approximation the equations of motion are after Newkirk whose work can be summarized as follows:

$$m\dot{u} = \pi r^2 P \tag{3.6}$$

$$m\dot{w} \sim 0 \tag{3.7}$$

where P is the pressure exerted by the resisting medium. For debris expelled initially radially, integration of the equations of motion leads to a cometlike cloud of material trailing off in the -u direction. Particles ejected with initial velocity components u_o and w_o are considered to reside in the neighborhood of the spacecraft for a characteristics time, τ and within a characteristic radius R_M from the center of the spacecraft of "radius", R_S

where

$$\tau = \frac{u_o}{\dot{u}} \tag{3.8}$$

After this interval, τ, particles have receded distances

$$R_u = \frac{u_o^2}{2\dot{u}} + R_S \tag{3.9}$$

in the u direction and

$$R_w = \frac{2u_o^2}{\dot{u}} + R_S \tag{3.10}$$

in the w direction. The characteristic radius is thus taken as

$$R_M = \frac{u_o^2}{\dot{u}} + R_S \tag{3.11}$$

Note that τ is just the time required for the drag force to stop a particle (relative to the spacecraft) which was initially ejected "into the wind." The criterion for residence is, thus, that the center of mass of the debris ejected at a particular time have the same velocity as the spacecraft rather than the debris being within some artibrary distance. Within R_M spherical symmetry of debris about the satellite is assumed to remain relatively unaltered.

Table 3.1 may be used to calculate the residence times, τ, for some representative particles. For $u_o = 7 \times 10^2$ cm/sec and r = 100μ, (see below), $\tau \sim 17$ sec for the Gemini satellite, while for the Apollo in its higher orbit, $\tau \sim 400$ sec. For the same circumstances, $R_M \sim 10^4$ cm and 3×10^5 cm, respectively. A similar particle ejected from an Apollo in a synchronous orbit would, according to this model, accompany the spacecraft for $\tau \sim 2 \times 10^5$ sec with $R_M \sim 10^8$ cm. It is seen that even in the presence of aerodynamic drag, much of the cloud of expelled debris will accompany a satellite for considerable intervals even though it will tend to expand with a velocity close to that of the initial ejection. In interplanetary space where radiation pressure is the primary accelerator, the debris orbits with the satellite for days or even weeks and the cloud may extend over hundreds of kilometers.

The mass per unit column of particles of radius r may be calculated on the basis of a constant radial velocity u_o to be

$$M_S(r) = \frac{\left(\frac{dm}{dt}\right)}{4\pi u_o}\left(\frac{1}{R_S} - \frac{1}{R_M(r)}\right) \tag{3.12}$$

$$\text{for } R_M \gg R_S: \; M_S(r) = \frac{\frac{dm}{dt}}{4\pi\, u_o\, R_S} \tag{3.12a}$$

where $R_M(r)$ is the limit of the cloud for particles of radius r. For a pulse release the column density is given by

$$M_S = \frac{\Delta m}{4\pi u_o^2 t^2} \quad t < \tau \tag{3.13}$$

$$= 0 \qquad t \geq \tau$$

where τ is given in Equation (3.8). The above model can be used as a first approximation to the behavior of particulate matter in the environs of a spaceship. It is deficient in that it does not really allow for the effect of deceleration except in the calculation of the gross parameter, τ, (residence time) and R_M, a characteristic radius. More advanced models which allow for asymmetry of distribution should be developed.

3.1.1.3 Numerical Calculation of Model

The calculated drag (cm/sec^2), the characteristic or residence time, τ (sec), and the cloud size, $R_M - R_S$(cms) are presented in Table 3.2 for three altitudes, 160 km, 320 km, and 4 x 10^4 km. At two lower altitudes the drag is due to aerodynamic forces while at the highest altitude it is due to radiation pressure. The calculations are also made for two initial velocities, $u_{o1} = 3 \times 10^4$ cm/sec and $u_{o2} = 7 \times 10^2$ cm/sec.

Calculated values of the integrated mass per square centimeter are presented in Table 3.3 for various release rates, $\frac{dm}{dt}$ (gm/sec). Also furnished are N_S the integrated number of particles per square centimeter for different size particles. The calculations are made for two different values of the initial velocity, u_o. As can be seen from Equation (3.14) M_S is independent of altitude (for $R_M \gg R_S$) and depends only on the mass emission rates, the particle emission velocity, and the satellite size.

In addition, in Tables 3.4A and 3.4B there is calculated M_S, the integrated mass per cm^2 column for sudden impulsive releases of Δ m mass as a function of time for two different initial velocities.

TABLE 3.2

CALCULATION OF $\dot{u}$ (cm/sec^2), τ(sec) and R_M-R_S(cms) FOR VARIOUS ALTITUDES AND SIZE PARTICLES, (u_{o1} = 3 x 10^4 cm/sec; u_{o2} = 7 x 10^2 cm/sec, ρ = 1 gm/cm^3, v = 7.5 km/sec) for continuous release

A. Aerodynamic Drag, h = 160 km, $\rho_a = 10^{-12}$ gm/cm^3

r (microns)	$\dot{u}$ (cm/sec^2)	τ (seconds) (for u_{o1})	τ (seconds) (for u_{o2})	R_M-R_S (cm) (for u_{o1})	R_M-R_S (cm) (for u_{o2})
0.1	4.2×10^4	0.7	1.6×10^{-2}	2.14×10^4	1.1×10^1
1.0	4.2×10^3	7.0	1.6×10^{-1}	2.1×10^5	1.1×10^2
3.0	1.4×10^3	2.1×10^1	4.8×10^{-1}	6.3×10^5	3.4×10^2
1.0×10^1	4.2×10^2	7.0×10^1	1.6	2.1×10^6	1.1×10^3
1.0×10^2	4.2×10^1	7.0×10^2	1.6×10^1	2.1×10^7	1.1×10^4

B. Aerodynamic Drag, h = 320 km, $\rho_a = 4 \times 10^{-14}$ gm/cm^3

0.1	1.7×10^3	1.8×10^1	4.1×10^1	5.4×10^5	2.9×10^2
1.0	1.7×10^2	1.8×10^2	4.1	5.4×10^6	2.9×10^3
3.0	5.7×10^1	5.3×10^3	1.2×10^1	1.6×10^7	8.5×10^3
1.0×10^1	1.7×10^1	1.8×10^3	4.1×10^1	5.4×10^7	2.9×10^4
1.0×10^2	1.7	1.8×10^4	4.1×10^2	5.4×10^8	2.9×10^5

C. Radiation Pressure, h = 4×10^4 km

0.1	3.4	9×10^3	2.1×10^2	2.7×10^8	1.5×10^5
1.0	3.4×10^{-1}	9×10^4	2.1×10^3	2.7×10^8	1.5×10^6
3.0	1.1×10^{-1}	3×10^5	6.4×10^3	9×10^9	4.5×10^6
1.0×10^1	3.4×10^{-2}	9×10^5	2.1×10^4	2.7×10^{10}	1.5×10^7
1.0×10^2	3.4×10^{-3}	9×10^6	2.1×10^5	2.7×10^{11}	1.5×10^8

TABLE 3.3

CALCULATION OF M_s (MASS LOADING PER cm^2) AND N_s (NUMBER OF PARTICLES/cm^2) USING EQUATION 3.12 FOR CONTINUOUS RELEASE

A. $R_s = 2 \times 10^2$ cm, $\mu_{01} = 3 \times 10^4$ cm/sec

$\frac{dm}{dt}$ (gms/sec)	M_s (gm/cm^2)	N_s (total number of particles per cm^2) r = 0.1 (micron)	1.0 (micron)	3.0 (micron)	1.0×10^1 (micron)	1.0×10^2 (micron)
1.0	1.30×10^{-8}	3.1×10^6	3.1×10^3	1.2×10^2	3.1	3.1×10^{-3}
10^{-1}	1.30×10^{-9}	3.1×10^5	3.1×10^2	1.2×10^1	3.1×10^{-1}	3.1×10^{-4}
10^{-2}	1.30×10^{-10}	3.1×10^4	3.1×10^1	1.2	3.1×10^{-2}	3.1×10^{-5}
10^{-3}	1.30×10^{-11}	3.1×10^3	3.1	1.2×10^{-1}	3.1×10^{-3}	3.1×10^{-6}

B. $R_s = 2 \times 10^2$ cm , $\mu_{02} = 7 \times 10^2$ cm/sec

1.0	5.6×10^{-7}	1.3×10^8	1.3×10^5	4.8×10^3	1.3×10^2	1.3×10^{-1}
10^{-1}	5.6×10^{-8}	1.3×10^7	1.3×10^4	4.8×10^2	1.3×10^1	1.3×10^{-2}
10^{-2}	4.5×10^{-9}	1.3×10^6	1.3×10^4	4.8×10^1	1.3	1.3×10^{-3}
10^{-3}	5.6×10^{-10}	1.3×10^5	1.3×10^2	4.8	1.3×10^{-1}	1.3×10^{-4}

TABLE 3.4A

CALCULATION OF M_s (INTEGRATED MASS PER cm^2 COLUMN) FOR SUDDEN IMPULSIVE RELEASE OF Δm MASS AS A FUNCTION OF TIME (sec)

Δm (gms) \ t (sec)	10^{-3}	10^{-2}	10^{-1}	1	10	10^2	10^3	10^4	10^5
10^{-3}	9×10^{-8}	9×10^{-10}	9×10^{-12}	9×10^{-14}	9×10^{-15}	9×10^{-18}	9×10^{-20}	9×10^{-22}	9×10^{-24}
10^{-2}	9×10^{-7}	9×10^{-9}	9×10^{-11}	9×10^{-13}	9×10^{-15}	9×10^{-17}	9×10^{-19}	9×10^{-21}	9×10^{-23}
10^{-1}	9×10^{-6}	9×10^{-8}	9×10^{-10}	9×10^{-12}	9×10^{-14}	9×10^{-16}	9×10^{-18}	9×10^{-20}	9×10^{-22}
1	9×10^{-5}	9×10^{-7}	9×10^{-9}	9×10^{-11}	9×10^{-13}	9×10^{-15}	9×10^{-17}	9×10^{-19}	9×10^{-21}
10	9×10^{-3}	9×10^{-6}	9×10^{-8}	9×10^{-10}	9×10^{-12}	9×10^{-14}	9×10^{-16}	9×10^{-18}	9×10^{-20}
10^2	9×10^{-3}	9×10^{-5}	9×10^{-7}	9×10^{-9}	9×10^{-11}	9×10^{-13}	9×10^{-15}	9×10^{-17}	9×10^{-19}
10^3	9×10^{-2}	9×10^{-4}	9×10^{-6}	9×10^{-8}	9×10^{-10}	9×10^{-12}	9×10^{-14}	9×10^{-16}	9×10^{-18}

$$M_s = \frac{1}{4\pi\mu_o^2} \frac{\Delta m}{t^2}, \quad \mu_{01} = 3 \times 10^4 \text{ cm/sec}; \quad M_s = 9 \times 10^{-11} \frac{\Delta m}{t^2}$$

TABLE 3.4B

SAME AS TABLE 4A EXCEPT CALCULATION MADE FOR $\mu_{02} = 7 \times 10^2$ cm/sec

Δm (gms) \ t(sec)	10^{-3}	10^{-2}	10^{-1}	1	10	10^2	10^3	10^4	10^5
10^{-3}	1.6×10^{-4}	1.6×10^{-6}	1.6×10^{-8}	1.6×10^{-10}	1.6×10^{-12}	1.6×10^{-14}	1.6×10^{-16}	1.6×10^{-18}	1.6×10^{-20}
10^{-2}	1.6×10^{-3}	1.6×10^{-5}	1.6×10^{-7}	1.6×10^{-9}	1.6×10^{-11}	1.6×10^{-13}	1.6×10^{-15}	1.6×10^{-17}	1.6×10^{-19}
10^{-1}	1.6×10^{-2}	1.6×10^{-4}	1.6×10^{-6}	1.6×10^{-8}	1.6×10^{-10}	1.6×10^{-12}	1.6×10^{-14}	1.6×10^{-16}	1.6×10^{-18}
1	1.6×10^{-1}	1.6×10^{-3}	1.6×10^{-5}	1.6×10^{-7}	1.6×10^{-9}	1.6×10^{-11}	1.6×10^{-13}	1.6×10^{-15}	1.6×10^{-17}
10	1.6×1	1.6×10^{-2}	1.6×10^{-4}	1.6×10^{-6}	1.6×10^{-8}	1.6×10^{-10}	1.6×10^{-12}	1.6×10^{-14}	1.6×10^{-16}
10^2	1.6×10	1.6×10^{-1}	1.6×10^{-3}	1.6×10^{-5}	1.6×10^{-7}	1.6×10^{-9}	1.6×10^{-11}	1.6×10^{-13}	1.6×10^{-15}
10^3	1.6×10^2	1.6×1	1.6×10^{-2}	1.6×10^{-4}	1.6×10^{-6}	1.6×10^{-8}	1.6×10^{-10}	1.6×10^{-12}	1.6×10^{-14}

$$M_s = \frac{1}{4\pi\mu_o^2}\,\frac{\Delta m}{t^2} \;;\quad \mu_{02} = 7 \times 10^2 \text{ cm/sec};\quad M_s = 1.6 \times 10^{-7}\,\frac{\Delta m}{t^2}$$

N_S may be calculated from Tables 3.4A and 3.4B by dividing the volume of each particle.

The above tables render it relatively simple to determine the size and mass loading of clouds of particles created by the release of particles from spacecraft.

3.1.2 Theoretical Background of Optical Behavior

3.1.2.1 General Relations

The radiance of sunlight scattered by particles surrounding a satellite can be calculated on the assumption of a spherical cloud with a spherical satellite at the center outward flow of individual particles. Moreover, the radius of the cloud is taken as R_M as given by Equation (3.11). Consider a detector of area A with a solid angle of view ω_1 (Figure 3.2). The energy received from spherical particles of radius, r from the elementary, volume dV which contains m(R,r)g of particles/cm^3 with a scattering function (ϕ, r) per gram, is for small optical depth,

$$dE = F_\odot \; \sigma(\phi,r)\omega_2\omega_1 \; R^3 m(R,r) \; dR \; dr \tag{3.14}$$

where ω_2 is the solid angle subtended by the detector at the particle and ϕ is the scattering angle. Since $F_\odot = \omega_\odot B_\odot$, where

$\omega_\odot$ = solid angle subtended by the Sun,

$B_\odot$ = mean radiance of the solar disk,

the radiance of dV compared to that of the Sun is

$$\frac{dB}{B_\odot} = \omega_\odot \; \sigma(\phi,r)m(R,r) \; dR \; dr \tag{3.15}$$

or

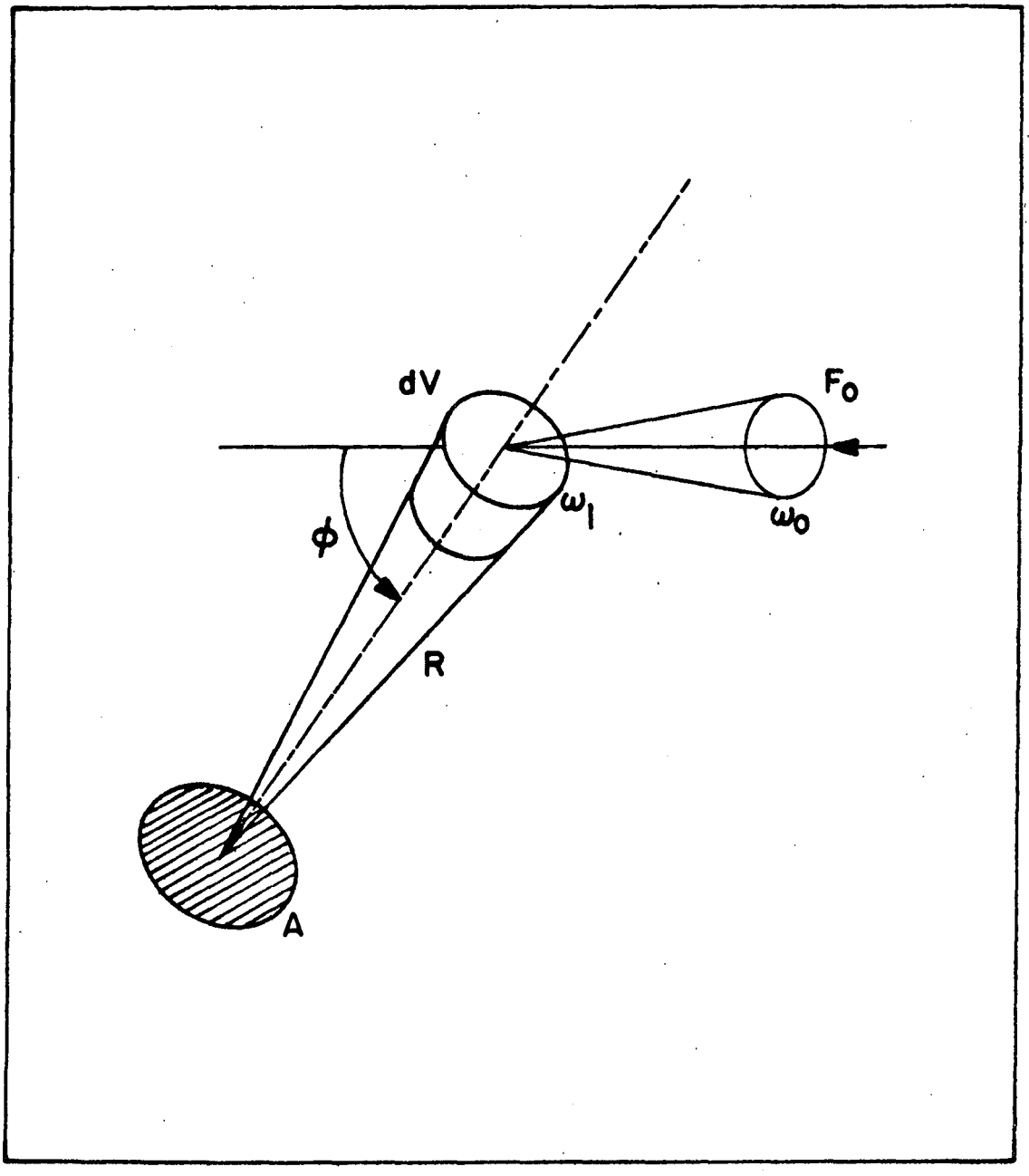

Figure 3.2 Geometry for calculation of the radiance of sunlit debris near a spacecraft. (Taken From Ref. 8).

$$\left(\frac{B}{B_\odot}\right)_\phi = \omega_\odot \int_{r_o}^{r_{max}} \sigma(\phi,r) \int_R^{R_M(r)} m(R,r)\, dR\, dr$$

Note that r_o and r_{max} represent the lower and upper limits of particle radii and that the second integral represents the mass of debris of particles of radius r in a 1 cm^2 column above the surface of a satellite.

The present case of interest involves monodispense particles so that a simplified formula may be written

$$\left(\frac{B}{B_\odot}\right)_\phi = \omega_\odot \quad (\phi)\ M_s \tag{3.16}$$

3.1.2.2 Numerical Calculations

There are many tabulations of Mie scattering calculations, Penndorf[27] and Denman et al,[28] Van de Hulst,[29] etc., and the theory by now is well substantiated. Angular scattering values for various angles for water drops (m = 1.33) are presented in Table 3.5 after Van de Hulst.[29] For x($\frac{2\pi a}{\lambda}$ where a = particle radius) large an approximation is used.

The general theory is now developed so that this table may be utilized. Calling the entries, T_p, (scattering function for a particle)

$$T_p = \frac{1}{2x^2} \left\{i_1(\theta) + i_2(\theta)\right\} \quad \text{, also} \tag{3.17}$$

TABLE 3.5

THEORETICAL VALUES OF $(1/2\ x^2)\left\{i_1(\theta) + i_2(\theta)\right\}$

for m = 1.33 (taken from Van de Hulst, Ref. 29)

x	a for $\lambda = 0.5\mu$	θ				
		0°	10°	30°	60°	Av. 90°–180°
0.6	0.048	0.0060	0.0059	0.0051	0.0035	0.0034
1.0	0.08	0.053	0.052	0.044	0.027	0.018
1.5	0.12	0.29	0.28	0.22	0.11	0.035
2.0	0.16	0.99	0.95	0.70	0.26	0.015
2.5	0.20	2.37	2.24	1.39	0.32	0.04
3.0	0.24	4.62	4.30	2.33	0.13	0.03
3.6	0.29	8.5	7.7	3.2	0.13	0.06
4.0	0.32	12.3	10.8	3.6	0.13	0.05
5.0	0.40	23.4	19.1	3.1	0.41	0.07
6.0	0.48	34.8	25.7	1.57	0.26	0.08
8.0	0.64	46.0	24.4	2.4	0.40	0.10
10.0	0.80	36	8.6	2.2	0.37	0.01
12.0	0.96	23	4.2	1.1	0.14	—
15.0	1.2	104	16.9	0.7	0.24	0.02
20.0	1.6	120	3.0	0.5	0.15	0.32
25.0	2.0	244	0.2	0.9	0.13	0.06
30.0	2.4	231	14.9	1.2	0.12	0.06
35.0	2.8	445	2.3	1.5	0.18	0.09
40.0	3.2	401	1.2	1.97	0.20	0.07
Large x (diffraction)		$x^2/4$	0	0	0	0
(geometrical optics).		4.09	3.37	1.15	0.11	0.05

$$\sigma_p = \frac{1}{2k^2} \left\{ i_1(\theta) + i_2(\theta) \right\} \text{ where} \tag{3.18}$$

$$k = \frac{2\pi}{\lambda} \text{ and hence } x = ka \text{ and}$$

$$\sigma_p = a^2 \, T_p \text{ for a particle} \tag{3.19}$$

On a mass basis (per gram)

$$\sigma_g = \frac{\sigma_p}{\frac{4}{3}\pi a^3} = \frac{3}{4\pi a} \, T_p \; (\sigma_g = \sigma(Q,r)) \tag{3.20}$$

$$\sigma_g = \frac{.24}{a} \, T_p \tag{3.20a}$$

Hence substituting in Equation (3.16)

$$\frac{B(\theta)}{B_\odot} = \omega_\odot \left(\frac{.24}{a} \, T_p \right) M_s \tag{3.21}$$

As an aid in calculation since $\omega_\odot = 2.7 \times 10^{-4}$, and $F_\odot = 5 \times 10^{-2}$ watts/ cm^2 (between 4000 and 7000Å)

$$B_\odot = \frac{F_\odot}{\omega_\odot} = 1.85 \times 10^2 \text{ watts/cm}^2 \tag{3.22}$$

and

$$B(\theta) = \frac{1.2 \times 10^{-2}}{a} \, T_p \, M_s \tag{3.23}$$

Integration of Equation (3.13) yields the energy received at a detection as

$$E = BA\omega_1 = \frac{1.2 \times 10^{-2}}{a} \quad T_p \; M_s \; A\omega_1 \tag{3.24}$$

where A and ω_1 have been defined previously. For example in Table 3.6, there is calculated the brightness as a function of angle for selected angles for $M_s = 2 \times 10^{-9}$ making use of the data of Table 3.5.

As a matter of reference for Table 3.6 it should be noted that to obtain values of $\frac{B}{B_\odot}$ the tabulated values should be divided by 1.85×10^2. Also B for the radiance of the solar corona and zodiacal light varies from approximately 3.7×10^{-7} to 1.85×10^{-11} watts/cm^2 over 1° to 100°, respectively, from the Sun.

M_s of course, may be calculated from Equation (3.12) as illustrated in Table 3.3. A simple multiplication by

$$\frac{M_s}{2 \times 10^{-9}}$$

is adequate to convert the brightness in Table 3.6 to the corresponding brightness for the corresponding particle mass. For values of x not included, recourse must be made to the tabulation mentioned above or to the basic theory given for example in Van de Hulst.

It is noted that the M_s given in the tables are calculated on the basis of a 4π steradian release. Should a release be made in Ω steradians then M_s (if the release is in the forward direction) is increased in the ratio $\frac{4\pi}{\Omega}$ if $\frac{dm}{dt}$ remains constant.

3.2 Theory and Calculation of Released Gas Behavior

3.2.1 Theory Background

An analysis of the deficiencies of effused gas theory is presented below as well as a condensed description of this theory and specific parameterized calculations suitable for experimental design.

TABLE 3.6

CALCULATIONS OF BRIGHTNESS DUE TO ANGULAR MIE SCATTERING FOR $M_s = 2 \times 10^{-9}$ gms FOR SELECTED SIZE PARTICLES, MONODISPERSE IN DISTRIBUTION, IN SOLAR FLUX USING THE BASIC DATA IN TABLE 5

x	a for $\lambda=0.5\mu$	θ				
		0°	10°	30°	60°	Av. 90° - 180°
1.0	0.08	1.59×10^{-7}	1.56×10^{-7}	1.42×10^{-7}	9.1×10^{-8}	5.4×10^{-8}
1.5	0.12	5.8×10^{-9}	5.6×10^{-7}	4.4×10^{-7}	2.2×10^{-7}	7.0×10^{-8}
3.0	0.24	4.6×10^{-6}	4.3×10^{-6}	2.33×10^{-6}	1.3×10^{-7}	3.0×10^{-8}
6.0	0.48	1.7×10^{-5}	1.3×10^{-5}	7.8×10^{-7}	1.3×10^{-7}	4.0×10^{-8}
15.0	1.2	2.1×10^{-5}	3.4×10^{-6}	1.4×10^{-7}	4.8×10^{-8}	4.0×10^{-9}
30.0	2.4	2.3×10^{-5}	1.5×10^{-6}	1.2×10^{-7}	1.2×10^{-8}	6.0×10^{-9}

$$B(\theta) = C\, M_s\, T_p \qquad B(\theta) = \frac{1.2 \times 10^{-2}}{a} M_s\, T_p \qquad \text{where } C = \frac{1.2 \times 10^{-2}}{a}$$

$$\text{for } M_s = 2 \times 10^{-9} \qquad B(\theta) = \frac{2.4 \times 10^{-11}}{a} T_p$$

3.2.1.1 Deficiencies

Existing theory of which that of Scialdone[18] is the most useful for computation suffer from various defects. First, the analysis is in general restricted to the material effused in the forward direction of the satellite trajectory and consequently little information is available on the off-axes component or shape of the effused molecular cloud. Second, a gross simplification is made that each collision results in a halving of the velocity. However, the well known analysis of rigid sphere elastic scattering yields a law in which both the change in velocity and the phase function of the scatterer depend on the mass ratio of the particles. Moreover, the atmospheric mean molecular weight varies with altitude from M = 26.7 at 160 km to M = 21.2 at 350 km. Further, at higher altitudes the dominant species becomes atomic oxygen, M = 16, and at still higher heights M = 1. Such diminished atmospheric molecular weight results in perserveration of velocities and highly diminished back scattering. Consequently, the use of simple mean free path calculations is not accurate.

3.2.1.2 Existing Theory (After Scialdone[18]

3.2.1.2.1 General Considerations

The molecules emitted by the spacecraft travel a mean distance, λ_D before colliding with ambient molecules. This distance is less than λ_o the normal atmospheric mean free path because the spacecraft is moving rapidly after the outgoing molecule. In the forward direction

$$\lambda_D = \frac{v_D}{v_0 + v_D} \lambda_0 , \tag{3.25}$$

where υ_D = desorbed molecule velocity

υ_o = satellite velocity

while at right angles

$$\lambda_D = \frac{v_D}{\sqrt{v_D^2 + v_0^2}} \lambda_o \tag{3.26}$$

For near-earth orbits, $\upsilon_D \ll \upsilon_o$. Hence, the two expressions practically coincide, and for simplicity, Equation (3.25) can be used in the calculations. This expression fulfills the conditions for a stationary spacecraft since the mean free path of the desorbed molecules, λ_D is equal to λ_o. The relative mean free path is then given in Figure 3.3 from Scialdone. The value for the orbital velocity was obtained from

$$v_0 = \sqrt{\frac{r_0}{r}} \sqrt{g_0 r_0} = 7.9 \sqrt{\frac{r_0}{r}} , \qquad (\text{km-s}^{-1}) \tag{3.27}$$

where g_0 is the acceleration of gravity, r_0 is the radius of the earth, and r is the radius of the orbit from the center of the earth. The velocity of the desorbed molecules can be calculated for near space properties using:

$$v_D = \sqrt{\frac{8\,KT}{\pi M}} \approx 4 \times 10^4 \text{ cm-s}^{-1} \tag{3.28}$$

Therefore, for the values of υ_0 experienced in near space, the relative free path is approximately 1/20 of the ambient mean free path.

3.2.2 Density of the Effusing Molecules

Assuming that the density of the molecules originating from a spherical spacecraft is such that the majority of the molecules do not collide with each other, and assuming that the trajectory is straight until the collision with ambient molecules, one obtains for the density of such molecules.

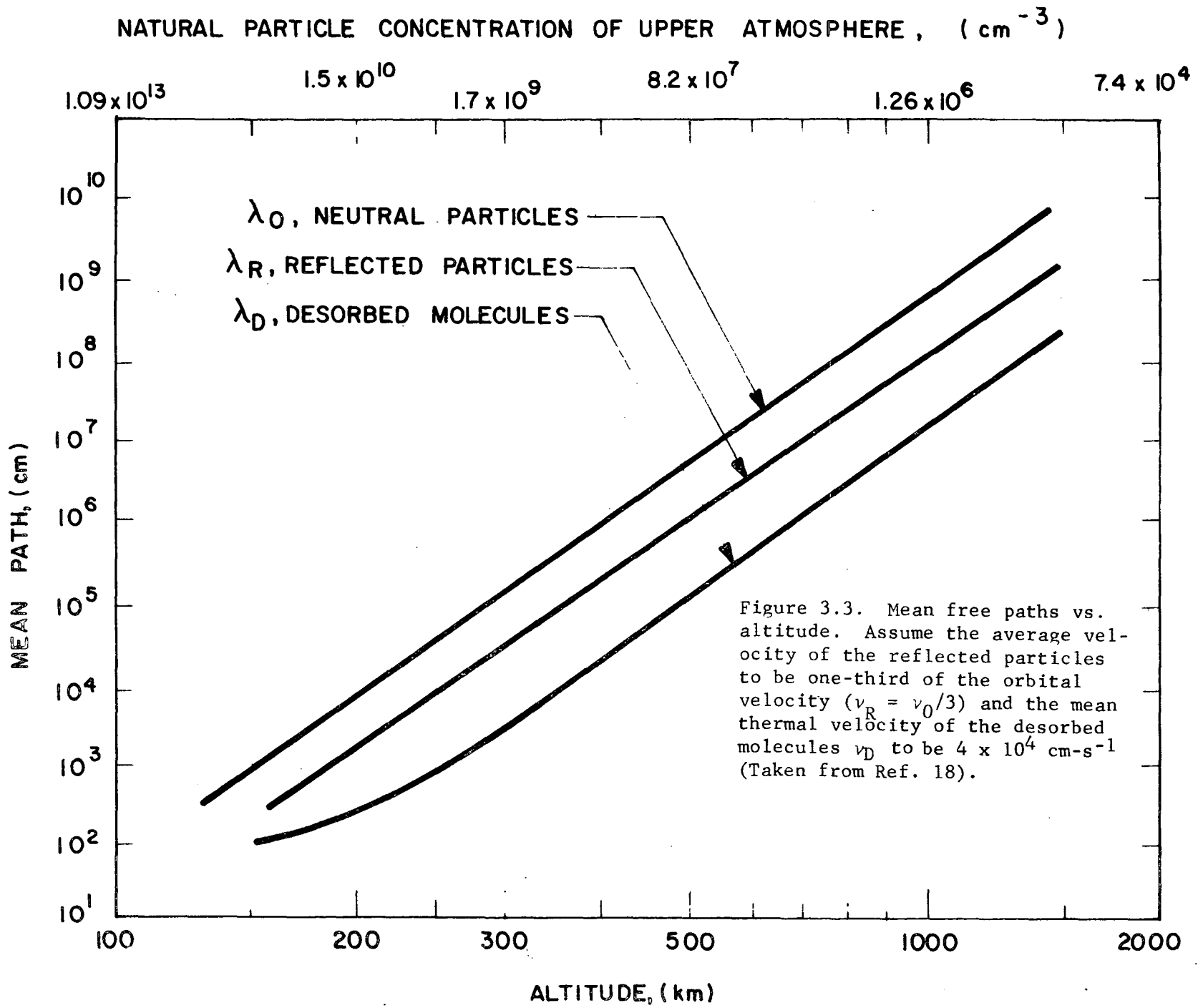

Figure 3.3. Mean free paths vs. altitude. Assume the average velocity of the reflected particles to be one-third of the orbital velocity ($v_R = v_0/3$) and the mean thermal velocity of the desorbed molecules v_D to be 4×10^4 cm-s^{-1} (Taken from Ref. 18).

$$n = \frac{N_D \; e^{\frac{x}{\lambda}}}{4\pi(R + x)^2 \; \upsilon_m} \tag{3.29}$$

At the surface of the spacecraft (i.e., x = 0), the density of the molecules leaving the spacecraft is

$$n_{x=0} = \frac{N_D}{4\pi R^2 v_m} \tag{3.30}$$

3.2.2.1 Density of Returning Molecules

Molecules leaving the spacecraft with drift velocities equal to the vector sum of the spacecraft and desorption velocities collide, at some distance from the spacecraft, with ambient molecules which can be considered immobile. After collision, the drift velocity of these desorbed molecules is less than the spacecraft velocity.

The total number of these molecules N'' striking the unit surface of the spacecraft is the sum of the molecules at the various distances, $0 < x < \infty$, in front of the spacecraft; i.e.,

$$\begin{aligned} N'' &= \int_0^\infty dn = \int_0^\infty \frac{N_D e^{-x/\lambda}}{4\pi(R+x)^2\lambda} dx \\ &\approx \frac{N_D}{4\pi\lambda R} \quad \text{for } \lambda \gg R . \end{aligned} \tag{3.31}$$

At a distance, a in front of the satellite, the number of returning molecules is

$$N_a'' = \int_a^\infty dn = \int_a^\infty \frac{N_D e^{-x/\lambda}}{4\pi(R+x)^2\lambda} dx$$
$$= \frac{N_D}{4\pi\lambda} \frac{e^{-a/\lambda}}{(R+a)} . \tag{3.32}$$

Since the flux per unit area is $n'' \upsilon_n = N''$, the apparent density n'' is given by

$$n'' = \frac{N''}{\nu_n} = \frac{N_D}{4\pi\lambda\nu_n} \frac{1}{R} . \tag{3.33}$$

The integration in Equation (3.31) was performed for the molecules that suffer collision in front of the spacecraft along the axis of motion and in a unit cross-section column. Scattering has been disregarded under the assumption that molecules scattered out of the column are replaced by molecules scattered in from other columns. For collimated beams this assumption is erroneous.

3.2.3 Some Calculations

The above equations permit computation of various constants typical of the environment surrounding the spacecraft. With the appropriate value for λ and υ, the concentrations, pressures, and fluxes at various distances from an orbiting spacecraft can be calculated provided the ambient parameters and a knowledge of the molecules desorbed by the spacecraft are known. As will be shown, the optical thickness of the environment can also be calculated.

1. Desorbed Molecules--Forward Region

The concentration of the molecules uniformly outgassed from the surface of a spherical spacecraft at a distance, x from this surface is given by Equation (3.29). Inserting the value of

$\lambda = \lambda_D = [\nu_D/(\nu_0 + \nu_D)]\lambda_0$, the full equation is obtained

$$n_D = \frac{N_D}{4\pi\nu_D} \frac{\exp\left(-\frac{\nu_D + \nu_0}{\nu_D}\frac{x}{\lambda_0}\right)}{(R+x)^2} \qquad \text{(molecules-cm}^{-3}\text{)} \tag{3.34}$$

Parametric plots of this equation are shown in Figure 3.4. The value of υ_D, the thermal velocity of the desorbed molecules, has been maintained constant at 4×10^4 cm-s^{-1}. The orbiting velocity, υ_0 and the ambient mean free path are functions of altitude. Knowing N_D expressed in any form, the concentration can be read as a function of the distance, altitude, and size of the spacecraft. Figure 3.4 shows that at low altitude, the density resulting from outgassing products drops quite rapidly at a distance of about 10 cm from the spacecraft. At high altitudes, the drop is more gradual, becoming an order of magnitude lower at about 2 to 3 m from the surface.

2. Returning Molecules--Condensation Region

Equation (3.33) expresses the concentration of outgassed molecules that have collided with the ambient molecules and returned to the spacecraft. Substituting the value of $\lambda = \lambda_D = [\nu_D/(\nu_D + \nu_0)]\lambda_0$, it reduces to

$$\frac{n''}{N_D} = \frac{P''}{KTN_D} = \frac{1 + \frac{\nu_0}{\nu_D}}{4\pi R\lambda_0\nu_n} \qquad \text{(s-cm}^{-3}\text{)}, \tag{3.35}$$

also

$$\frac{n''}{n_D} = \frac{P''}{P_D} = \frac{R\left(\frac{\nu_0}{\nu_D} + 1\right)\nu_D}{\lambda_0\nu_n} \; . \tag{3.36}$$

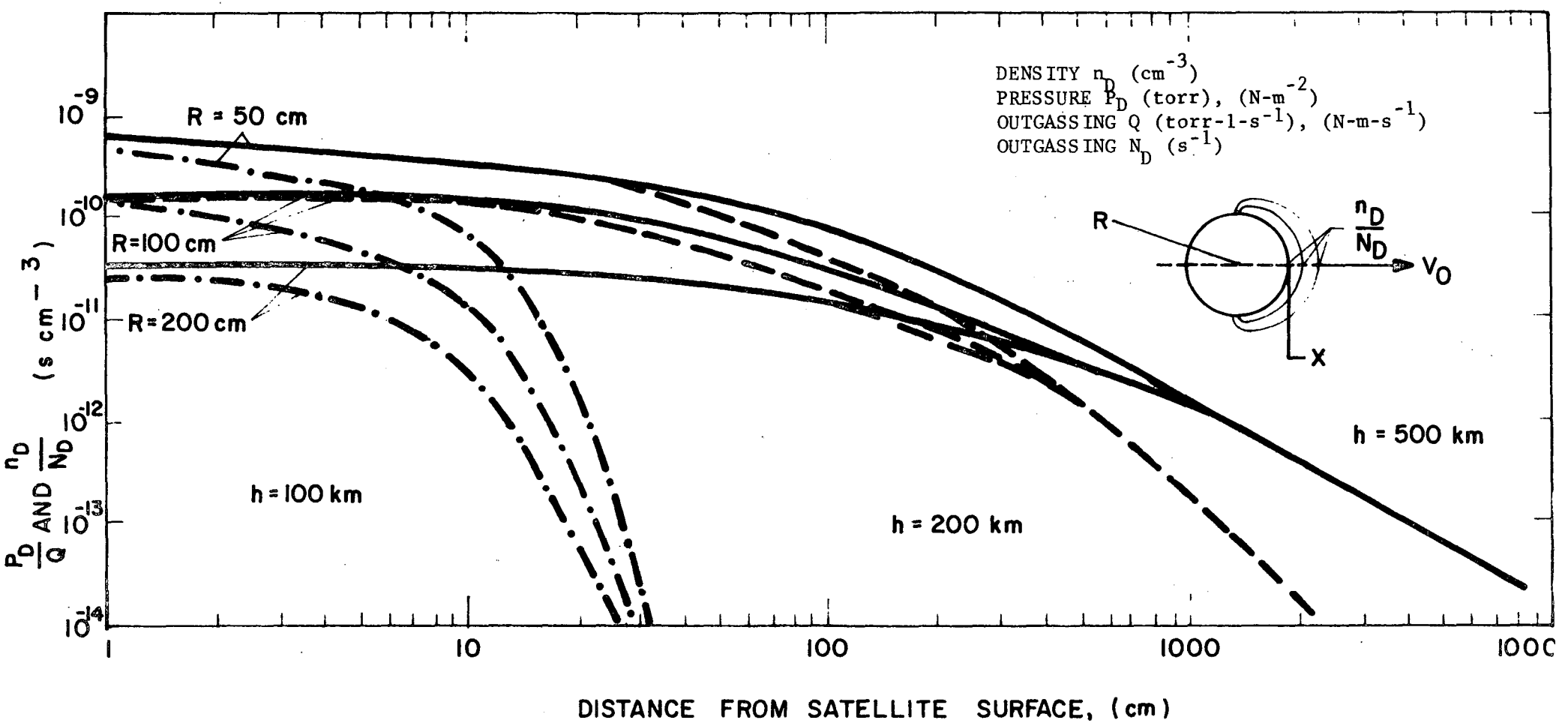

Figure 3.4. Pressure and density produced by outgassing vs. distance from the spacecraft surface (taken from Ref. 18)

In order to evaluate Equations (3.35) and (3.36), it is necessary to estimate the velocity of the returning molecules, υ_n. According to Reference 18, in an elastic collision with an environmental molecule which can be considered fixed, the molecule escaping the spacecraft surface loses, on the average, half of its velocity and, in inelastic collision, somewhat more. Because of this, the molecule either drops behind the satellite or is picked up if collision occurs close to the satellite and the molecule has time to reach the front surface. From this, and the fact that the escaping absolute velocity $\upsilon_0 + \upsilon_D$, one can estimate the velocity υ_n to be about $1/2\, \nu_0$. Figure 3.5 is a plot of Equation (3.35) using this value for υ_n. Figure 3.5 is a plot of Equation (3.35) using this value for υ_n. It indicates that the returning density resulting from a known outgassing decreases quite rapidly with altitude and becomes roughly constant at altitudes in excess of 1000 km. Also, the concentration is higher for smaller spacecraft diameters.

Figure 3.6 is a plot of Equation (3.36), again using $\nu_n = 1/2\ \nu_0$. As expected, the density ratio at the surface decreases rapidly with altitude, reaching a practically constant value at 1000 km or more, and increases with the radius.

Figure 3.5 shows also the flux of the returning molecules as a function of the altitude and spacecraft radius. Knowing the outgassing value (N_D), this flux, which under appropriate conditions can be the source of contamination, can be determined. Again, it is very much a function of altitude, becoming practically constant and apparently small at altitudes greater than 1000 km. Also, large spacecraft have a smaller return flux than smaller ones.

3.2.3.1 Rarefaction Region Behind Spacecraft

A rarefaction region is created behind a moving spacecraft by the sweeping action of the vehicle. This region increases with increasing spacecraft speed, υ_0 and is given approximately by Reference 18.

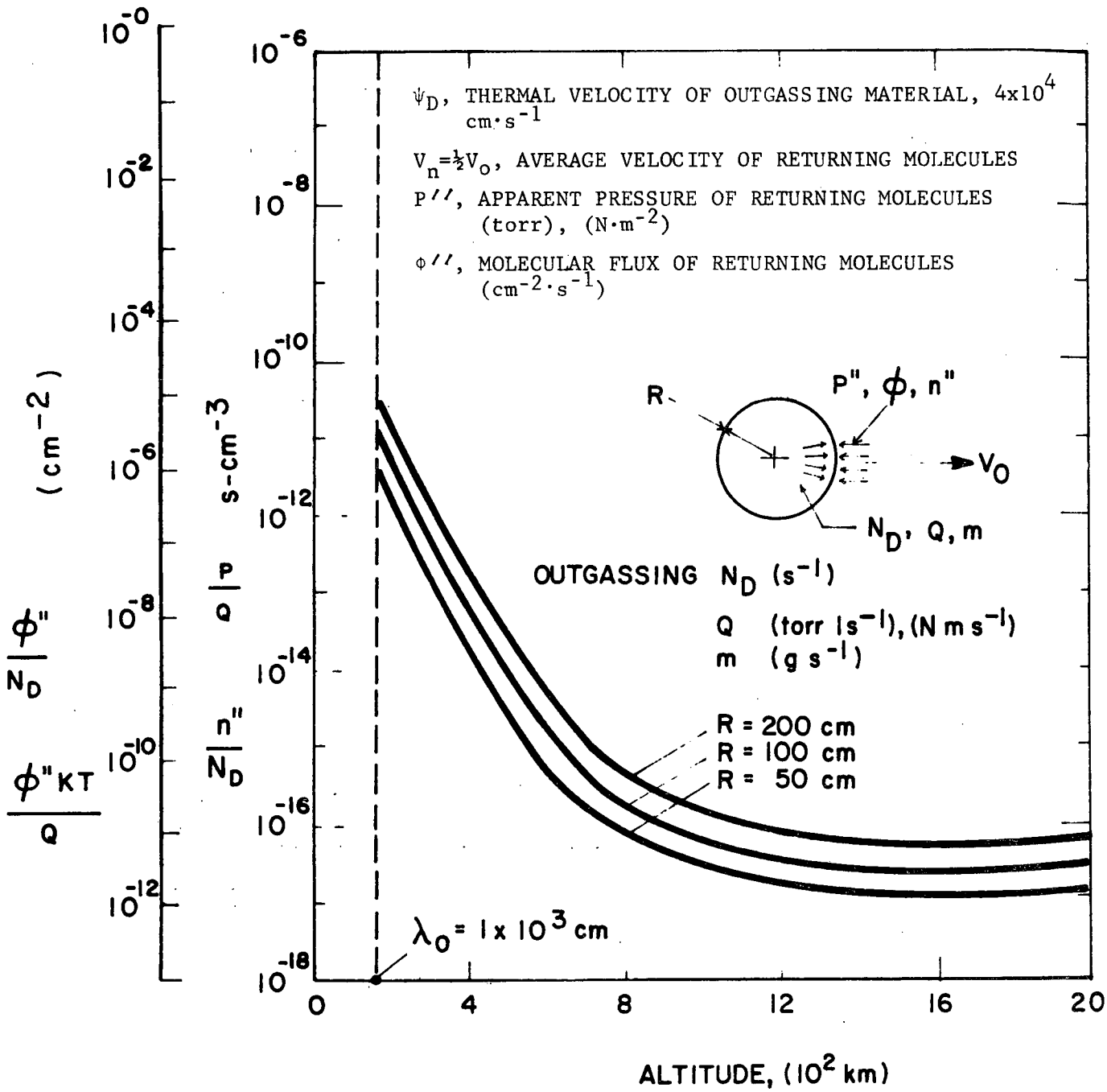

Figure 3.5. Density, pressure, and flux at the spacecraft surface, produced by outgassed molecules returning to the spacecraft, vs. altitude (for $\lambda_0 > 21R$) (taken from Ref. 18).

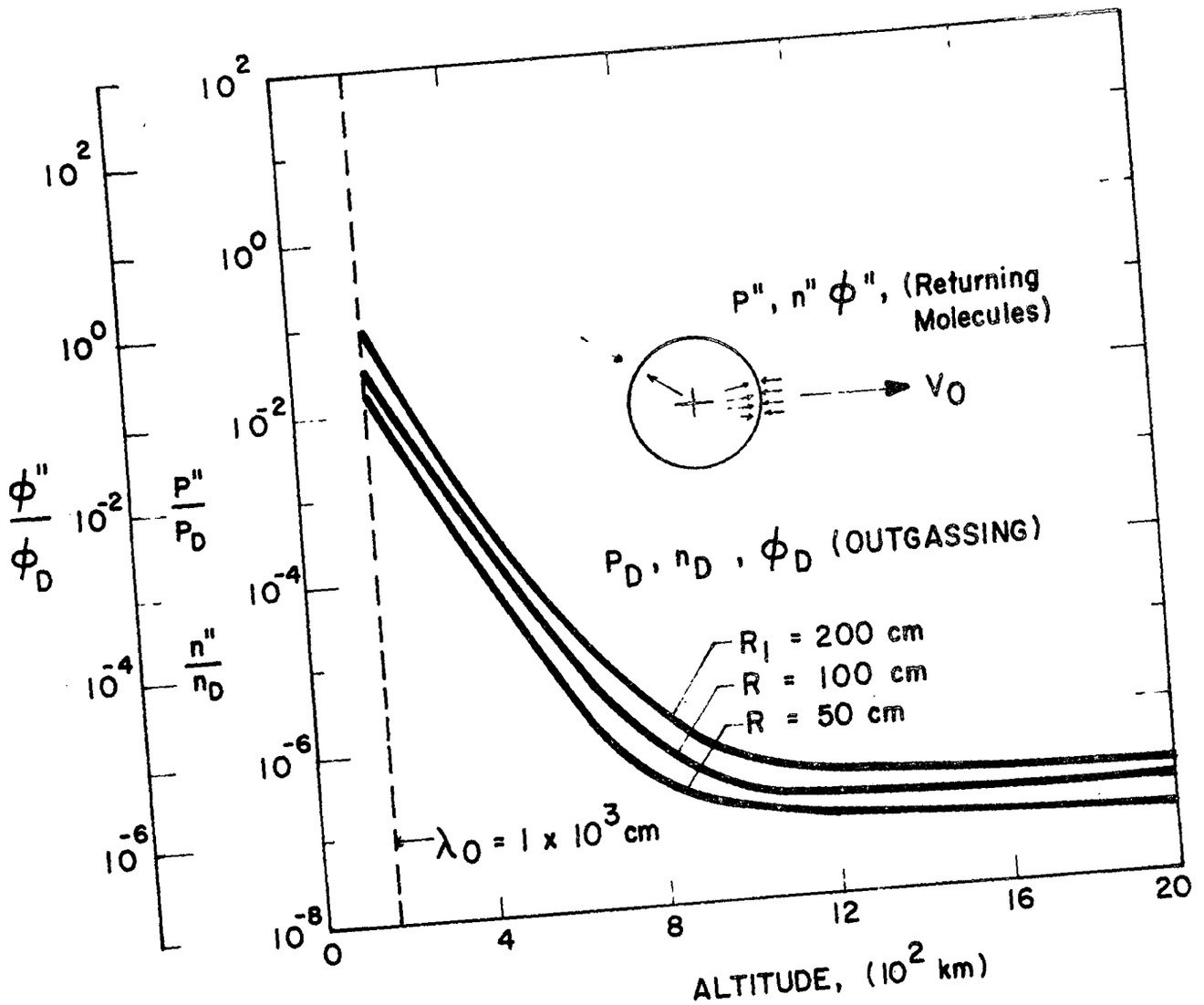

Figure 3.6. Density, pressure, and flux ratios at the spacecraft surface, produced by outgassed molecules returning to the satellite (for $\lambda_0 > 21R$) (taken from Ref. 18).

$$d \approx R \frac{v_0}{v}, \tag{3.37}$$

where $v = \sqrt{2KT/M}$ is the probable thermal velocity of the ambient molecules. Assuming a Maxwellian velocity distribution of the ambient molecules, the following exponential function for the density along the axis of motion and behind the spacecraft pertains

$$\frac{n}{n_0} = \exp\left[-\frac{Mv_0^2}{2KT}\left(\frac{R}{x}\right)^2\right] \tag{3.38}$$

This expression yields the following density ratios for a vehicle moving at $\upsilon_0 = 8$ km-s^{-1} and ambient molecules moving at $\upsilon = 1$ km-s^{-1}.

Distance (x/R)	Density (n/n_0)
5	0.1
10	0.5
15	0.75
25	0.9

This indicates that the mean free path in the rarefaction region is considerably higher (an order of magnitude) than the undisturbed value.

3.2.4 Optical Behavior

3.2.4.1 Resonance Light Scattering from Release Atomic (Molecular) Species

Optical resonance scattering from a released molecular cloud is a very strong phenomenon with cross-section which can be as large as 10^{-11} cm^2 and has consequently been used as an atmospheric probing process. The basic theory previously established is adapted below by computing the optical thickness.

Mass column density, M_s can be determined by integrating Equation (3.14) from zero to infinity. In fact, this equation, using $m(g\text{-}s^{-1}) = N_D M/A$ for the outgassing, yields (for $\lambda \geq R$)

$$M_S = \frac{\dot{m}}{4\pi v_m} \int_0^\infty \frac{e^{-x/\lambda}}{(R+x)^2}\, dx$$
$$\approx \frac{\dot{m}}{4\pi v_m} \frac{1}{R} \qquad (\text{g-cm}^{-2}). \tag{3.39}$$

This is the same expression obtained for particles ($R = R_S$). The product $M_s \sigma$ provides an explicit expression for the optical thickness of the molecular debris surrounding a spacecraft.

3.2.5 Calculations

For the case of steady release of gas molecules, the integrated amount of molecules is found in Table 3.7. (For different molecular weight multiply N_S by $\frac{18}{M}$, assuming υ_m constant.) In the case of an impulsive release the integrated number of molecules, for molecular weight M may be found by multiplying the tabulated numbers by $\frac{A}{M}$. For $M = 18$, $\frac{A}{M} = 3 \times 10^{22}$ for example.

It can be seen that for an atom where $\sigma = 10^{-11}$ cm^2 the continuous release of a milli-gram (10^{-3} gram) ($\sigma M_s \sim 1$) can yield a steady optically dense cloud around the spacecraft. For molecules with strong fluorescence at 10^{-17} cm^2 on the other hand 10^3 gms per second are required.

For the case of impulsive release, in Table 3.4A heavy lines indicate the length of time for a particular mass that the cloud remains optically thick (to left of heavy lines).

For experimental design the optical thickness as a function of $\frac{dm}{dt}$ is one of the basic parameters. An additional parameter is the size of the cloud. From Equation (3.29) and Figure 3.4, the profile

TABLE 3.7

CALCULATION OF INTEGRATED MASS (PER cm^2) AND INTEGRATED NUMBER OF MOLECULES FOR EFFLUENT GASES RELEASED AT STEADY RATE $\dot{m}$ (CALCULATED FOR H_2O, M=18)

Released Gas		Integrated Column Amount	
$\dot{m}$ (gms/sec)	N_D (molecules/sec)	M_s (gms/cm^2)	N_s (Molecules/cm^2)
1	3.3×10^{22}	1.3×10^{-8}	4.3×10^{14}
10^{-1}	3.3×10^{21}	1.3×10^{-9}	4.3×10^{13}
10^{-2}	3.3×10^{20}	1.3×10^{-10}	4.3×10^{12}
10^{-3}	3.3×10^{19}	1.3×10^{-11}	4.3×10^{11}
10^{-4}	3.3×10^{18}	1.3×10^{-12}	4.3×10^{10}
10^{-5}	3.3×10^{17}	1.3×10^{-13}	4.3×10^{9}
10^{-6}	3.3×10^{16}	1.3×10^{-14}	4.3×10^{8}

Calculated from formula

$$M_s = \frac{\dot{m}}{4\pi\ \nu_m R}\ ,\quad N_D = \dot{m}\,\frac{A}{M}\ ,\quad N_s = M_s\,\frac{A}{M}$$

$\nu_m = 3 \times 10^4$ cm/sec (same as μ_o for particles)

$R = 2 \times 10^2$ cm

M = 18 (molecule weight of water)

A = Avogadro's number

may be estimated to first order by assuming spherical symmetry and integrating line of sight for the intercept desired. As a crude estimate of cut-off from Figure 3.4, it can be seen that using the criterion of $n_D(r) = 10^{-3}\ n_D(o)$ this distance occurs at 20 to 30 cm from the satellite at 100 km, at approximately 1000 cm at 200 km and at approximately 5 to 10,000 cm (0.5 - 1.0 km) at 500 km altitude.

3.3 General Experimental Design Recommendations

The general theoretical experimental design for the two classes of experiments is presented below involving particulates and molecules.

3.3.1 Particulates

It is recommended that a range of separate monodisperse particle releases be made, for example, 0.1, 1.0, and 10.0 μm. Such releases will then enable the drag laws and previously developed models to be checked with regard to the size factor. Such releases should further be made over a range of altitudes which encompasses the space shuttle operating regime. In addition, with regard to the variation of drag with respect to direction of emission, some releases should be made in the forward direction of emission, and also in the backward direction of the rarefied regime. This will enable the check-out of the azimuth dependence. Relatively small amounts of material are required. For a steady-state release, the amount is less than 10^{-1}gm/sec for particles of 3 μm size (gives brightness greater than coronal and zodiacal light). For an impulsive release the mass for a reasonable period of observation of some 100 seconds is fairly large, of the order of a kilogram.

3.3.2 Atomic Resonance Gaseous Scattering

Again, here it is important that releases be made with different molecular masses particularly since the mass effect has been omitted in the current theory. Consequently, depending upon the experimental problems, releases of lithium and barium and perhaps an intermediate molecular weight such as sodium would be desirable.

Again, these releases should be made over the shuttle range of altitudes. Further, to check the variation of mean free path with azimuth of release, releases should be made at different angles with respect to the direction of motion. This will check the variation of mean free path with respect to angular variation. Also, some of the releases should be collimated in order to determine the degree and nature of scattering out of the beam and also the extent of backscattering.

The amount of material required is small being of the order of milligrams/sec for a steady release and of the order of 1 gm for impulsive releases lasting 100 seconds and of reasonable optical thickness. This fact suggests that there may be possible design techniques for controlled releases without the use of current cannisters. The goal should be to achieve a release technique which is safe and offers no hazard to the manned shuttle operations.

4.0 EXPERIMENTAL PROGRAM

4.1 SUGGESTED LASER PROBE TECHNIQUE FOR THE MEASUREMENT OF PARTICULATE MATTER IN THE VICINITY OF AN ORBITING SPACECRAFT

Particles generated by an operational spacecraft which remain in its vicinity can significantly interfere with and/or degrade experimental capabilities for specific classes of satellite airborne probes. Several sources for the generation and loss of the particulate matter have been itemized and discussed by others and assessed in Section 2 previously. Additionally, as discussed in Section 3, theoretical models have been developed to predict the concentration, size, spatial distribution, etc. of these materials. Finally, simulation chambers have also been employed to assist in the definition and solution of the problems associated with this phenomena. In any case, owing to significant disagreement and lack of laboratory data, the need for the performance of a systematic, reliable in situ measurement program appears evident. One of the initial experiments suggested for application to this program involves the utilization of an on-board laser system designed to yield reliable measurements with significant sensitivity on the presence, inventory, and distribution of particulate material in the vicinity of the spacecraft. In general the system design criteria have been adjusted so as to measure particle sizes and densities believed to be characteristic of the anticipated particulate cloud. Furthermore, the system has the capability of varying the position of the illuminated volume element so that positional scanning is available. Since a laser mode is employed, it can operate during daytime and/or nightside conditions for proper monitoring of the several possible operational functions for any selected portion of a given orbit.

The following experiment description is intended to be limited in scope but sufficient detail is included so as to demonstrate the feasibility of the proposed scheme and to demonstrate the potential experimental measurement capabilities involved.

4.2 GENERAL SYSTEM DESCRIPTION AND SIGNAL LEVEL CALCULATIONS

A concentric mode system (i.e. transmitter and receiver fields of view are congruent and therefore coaxial) is described first. This simplifies the exposition and also serves well to identify the limitations involved in a concentric mode and supply justification for employing a modified geometry. Following this, the proposed system will be described which employs an eccentric configuration. The several advantages of such a modification will become evident in the following discussions.

In the concentric mode, it can be shown that the Mie backscattered signal photon count, P_λ is given by:

$$P_\lambda = K\, C_\lambda\, \sigma\rho\delta t \text{ photons} \tag{4.1}$$

where C_λ is the output current in the laser beam (photons/sec) at wavelength (λ)

σ is the Mie backscattering cross section (cm^2/molecule)

ρ is the particle density (particles/cm^3)

δ is the duration of the photon output current in the laser beam

and K is given by:

$$K = \frac{T\, D^2}{8} \left[\frac{1}{R_1} - \frac{1}{R_2}\right] \quad \text{(cm)} \tag{4.2}$$

where T is the transmission factor of optical system

D is the diameter of receiver optics (cm)

R_1 is the minimum range noted above (cm)

R_2 is maximum range determined by gating cutoff time (cm)

The K-value represents the solution of an integral form which accounts for the geometry of the laser illuminated volume pulse within which the particles are considered to be homogeneously distributed.

The total number of photocathode electrons per pulse (assuming a multialkali PM tube of the low-noise, ruggedized variety such as an EMR 541-R or 641-R type) is given by:

$$E_\lambda = P_\lambda, Q_\lambda \tag{4.3}$$

where Q_λ is the PM quantum effieiency at λ.

A set of realistic system parameters is now considered as a preliminary design input:

C_λ = 11×10^{24} photons/sec at 6943Å (80 Millijoules/pulse with pulse duration of 25 nanoseconds)

σ = 10^{-9} - $10^{-11}/cm^2$ (as representative estimates for 1.0 - 0.2μ diameter particles, respectively)

ρ = 10^{-3} particles/cm^3 (selected to demonstrate system capability)

D = 35 cm

T = 25 percent (due to interference filter, reflection and absorption losses in optical systems, etc.)

R_1 = 15.2 meters (corresponds to 100 nanosecond delay)

R_2 = 152 meters

δt = 25 nanoseconds

Q_λ = 4.5 percent at 6943Å

Receiver optics: f/1.5 (i.e., 50 cm focal length)

Insertion of these values for the concentric mode into the above equations allows one to calculate the photocathode signal electron count. Substitution yields a result of 3×10^2 for a representative particle density of 10^{-3} cm^{-3} for a particle diameter of 1.0μ. This high count makes it evident then that the capability of detecting 10^{-3} cm^{-3} densities is relatively easily achieved especially for higher

laser power input levels and can result in the acquisition of reliable data. At this point, it is of interest to note that the laser light source divergence is expected to be of the order of 5 milliradians so that, in the concentric mode, the illuminated volume amounts to about 2×10^7 cm^3, so that it is justified to consider ρ-values of 10^{-3} (or less) cm^{-3}. On the other hand, such a large volume probe may be considered undesirable for certain applications. In the eccentric mode described below, the volume element can be readily adjusted and can be reduced to the order of only 10^3 cm^3 if desired.

It should be also noted that, in the present scheme, the receiver field of view is approximately four times greater than that required to overlap the sources; to decrease internal scattering. It should be pointed out, however, that this flexibility is achieved at the expense of vignetting the wanted light at the extreme ranges (i.e., in the vicinity of R_2). However, it is recalled from Equation (4.2) that loss of light at the further ranges is not as severe as loss of light at shorter ranges, owing to the fact that a hyperbolic relationship is involved.

The solid angle field of view is then

$$\Omega = \frac{\pi x\ (0.9)^2}{4 \times (51.3)^2} = 2.4 \times 10^{-4} \text{ steradian.}$$

For the orbiting vehicle configuration, an upper limit characteristic background encountered in the visible region of the spectrum is taken to be no greater than 1 Rayleigh/Å, or $10^6/4\pi$ photons/cm^2 sec ster Å. In order to reject the continum background the use of a narrow band filter placed ahead of the respective PM tubes is recommended. The filter can be peaked at the laser wavelength with transmission factors of approximately 50 percent or better. Assuming a $\Delta\lambda$ of 10Å filter, the background photoelectron count is given by:

$$E_b = \frac{10^6}{4\pi} \Omega \frac{\pi D^2}{4} \Delta\lambda \, TQ \, \Delta t \tag{4.4}$$

$$= 1.6 \times 10^{-4} \text{ electrons/pulse at } 6943\text{Å}$$

where Δt is the receiver gate time = 0.9 microseconds.

By comparing this value with the signal estimate given previously, it is seen that background radiation is of negligible importance. In fact, this calculation indicates that the field stop area could be increased considerably before this unwanted source becomes an important competing factor. It is noted here for future reference that this parameter is available for possible trade-off against other advantages that might be gained.

At this point, the gating problem alluded to earlier will be addressed. This is somewhat difficult to assess, since it involves a detailed knowledge of: (1) fall off with time of persistence after laser Q-switching has terminated, convolved with, (2) details of internal scattering by chamber walls and outgassing, etc., all of which combine to short-circuit the light path between source and detector. Since in the concentric mode these two are necessarily located in somewhat close proximity, the chances of short circuit paths are multiplied. It is worth noting in this connection that 10^{25} photons/sec (peak value) are emitted during the pulse and at a time of only 100 nanoseconds after initiation, one seeks to measure signal values several orders of magnitude less.

For this and other reasons, an alternate geometrical mode has been considered based on an off-axis scheme which greatly mitigates the problem. In this configuariton (termed here the eccentric mode), the source and detector are physically separated, so that internal short circuit paths are minimized. The eccentric mode, shown schematically in Figure 4.1, achieves the effect of range gating without recourse to the necessity of precise onset control, and obviates the

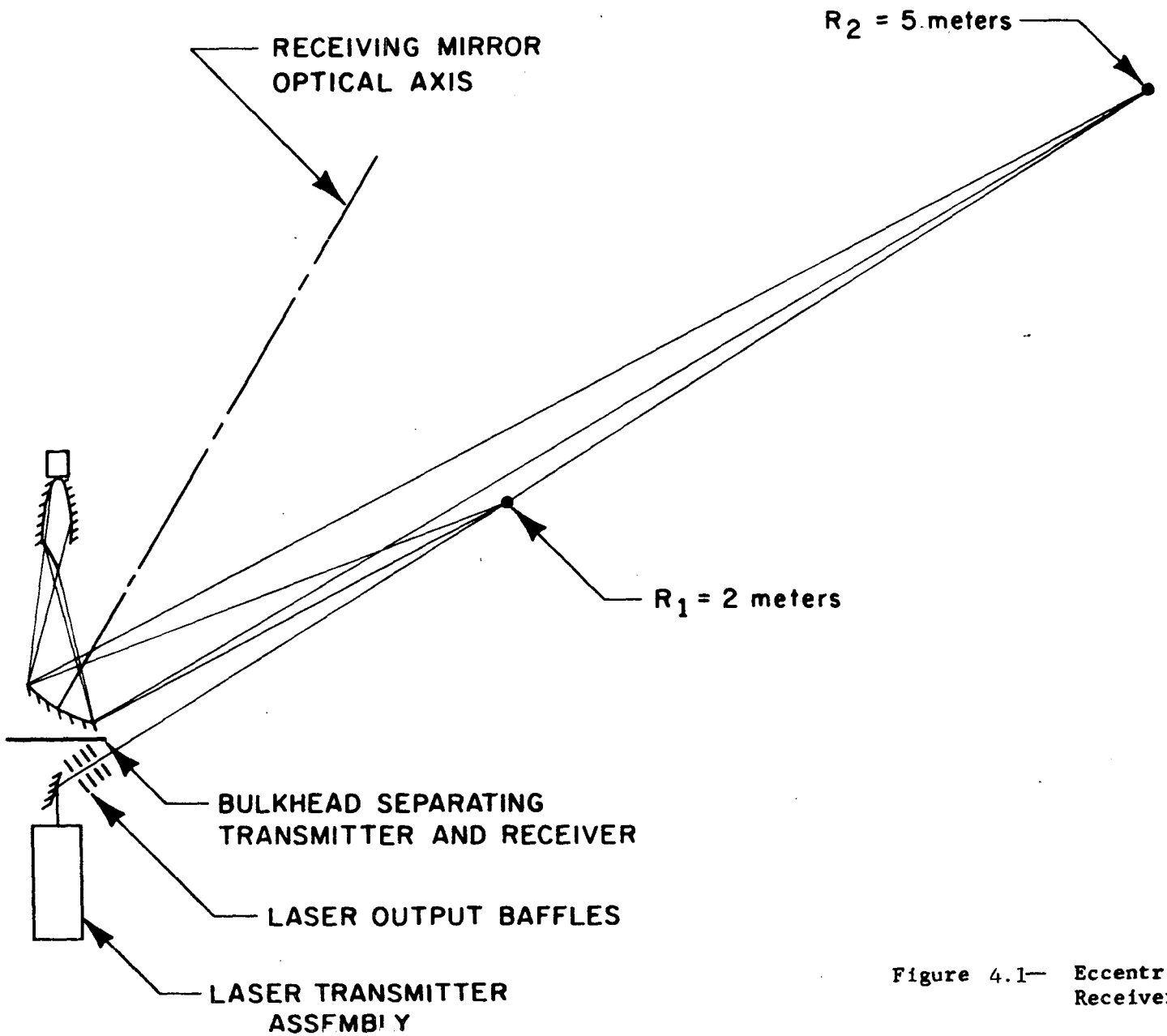

Figure 4.1— Eccentric Mode Laser/ Receiver Configuration

above-noted difficulties associated with laser cavity persistence effects. This provides a considerable net gain in terms of noise rejection and, hence, sensitivity. It should also be noted that the equations derived for the concentric mode are equally valid for the eccentric mode (apart from a cosine factor which is of minor importance and is thus ignored here).

An additional advantage accrues to the eccentric mode, in that a lesser minimum range can be accommodated. This, as can be seen from Equations (4.1) and (4.2) permits greater system sensitivity. Realistically, one can operate with a range of less than about 2 meters, which represents a distinct advantage for spatial scanning in the close vehicle vicinity. The maximum ranges are dictated by the maximum permissible size of the field stop. More specifically, the illumination beam, which is skewed with respect to the receiver optical axis, will be imaged in a line near the focal plane whose length is about 10 cm, and whose width is about 0.5 cm (which corresponds to the image thickness associated with the corresponding object width; i.e., the laser illumination beamwidth, whose divergence is about 5 mill-radians). A suitably oriented linear stop (as opposed to the circular field stop in the case of the concentric mode system) can be placed collinear with the image, and transfer of the received light from this somewhat odd-shaped field stop to the PM tube photocathode can be achieved by a suitable light guide arrangement behind the field stop. The required detector area is about of 5 to 10 cm^2. A suggested suitable optical configuration is shown in Figure 4.2. A more detailed description of characteristic suitable laser transmitter and receiver designs are given in Appendix B.

Calculations of expected signal levels have been performed for the eccentric mode geometry shown in Figure 4.1. These show that notwithstanding that a smaller volume element is illuminated by the laser (on the order of only 10^3 cm^3) the lower R_1 - value of only 2 meters more than offsets this factor so that the resultant photocathode signal electron counts are still greater than those of the concentric

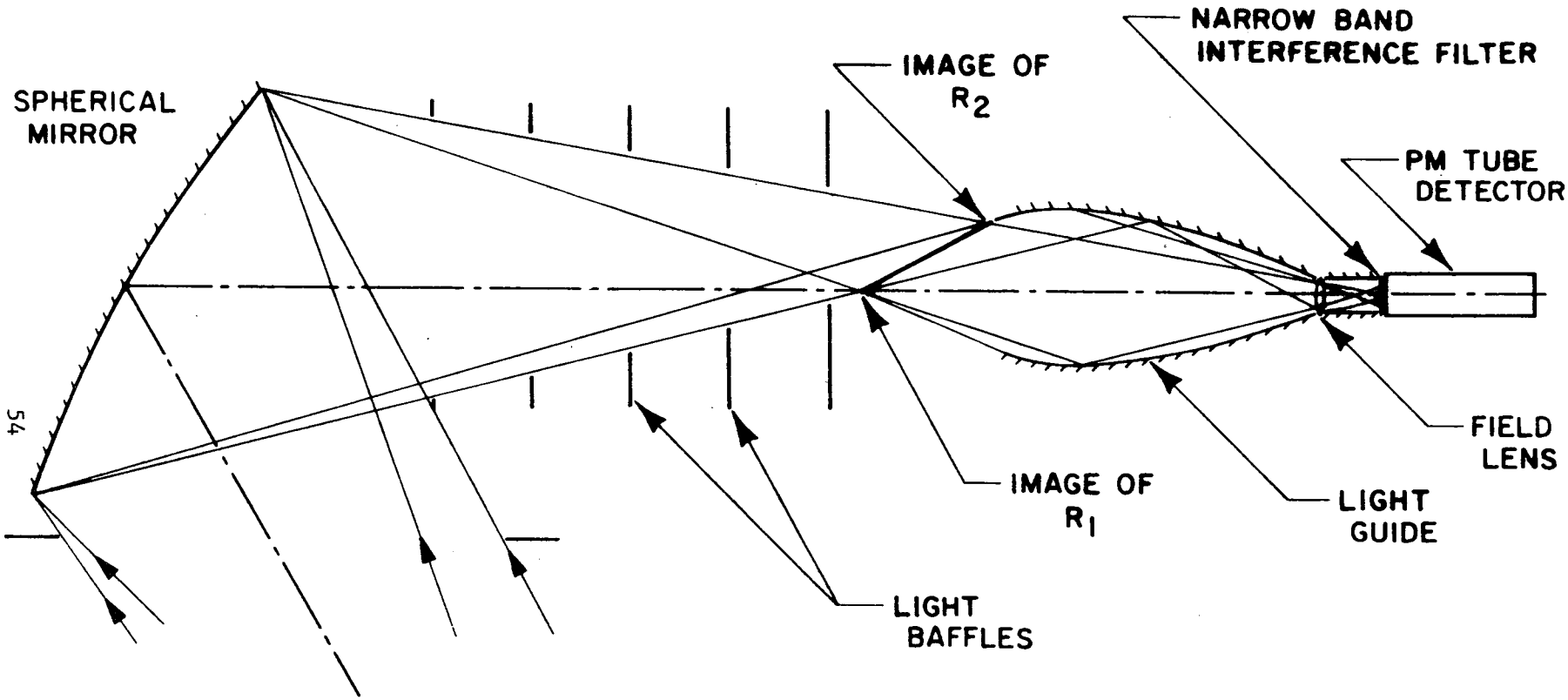

Figure 4.2— Suggested Optical Configuration to Accomodate the skewed beam and related imaging system geometry.

mode. Thus, in addition to other advantages the eccentric mode can provide even greater sensitivity than that indicated for the concentric mode. Furthermore, in the eccentric mode, gating is not essential since the deleterious effect of light in the near field is minimized owing to the more favorable geometry. This can be reduced further by activating the receiver only when an output pulse is generated. It will be possible, and indeed advisable, to synchronize the signal processing circuit with the laser Q-switch output pulse. The receiver turn-off can occur at any time after the laser light train passes beyond the range R_2. Since the background is negligible in the present case the precise turnoff time is not too critical.

The indicated sensitivity and flexibility of the eccentric mode is desirable since it facilitates varying the geometry of the overall system in order to systematically preselect the size, shape, and location of the illuminated volume element. In this manner, monitoring of particulates can be performed on preselected target areas at any time during orbit. In addition, such an operational mode provides backscatter data over a variety of scattering angles which are useful for particle size analysis. In combination with the above, a more precise particle size distribution can be determined within the preselected volume element if spectral diversity is applied. This presents no difficulty since present commercial dye laser technology can supply dye lasers with suitable characteristics which operate in the yellow (5700 - 6100Å), green (5100 - 5700Å), blue (4500 - 4600Å) and deep blue (4000 - 4300Å) spectral regions. In addition, it should be noted that the frequency doubled 3472Å ruby laser is also available. This wavelength regime selection corresponds to sub-micron particulates since size distribution data is optimum for α-values which vary between 3 - 6 where $\alpha = \pi d/\lambda$ (where d = particle diameter, λ = wavelength in equivalent units).

Owing to present laser technology it can be anticipated that lasers will be available to operate on selected resonance and/or fluorescence frequencies for essentially all regions in the visible

and near UV portions of the spectrum. Present day dye lasers are available currently with 0.1 Joule input and 0.1Å resolution. Additionally, it is reasonable to expect the availability of suitable lasers operating in the VUV and even EUV in the near future. Clearly, such modifications can result in the application of the selected satellite borne laser to a larger number and variety of earth atmospheric probe applications which are not discussed herein since it is considered to be outside of the scope of the present defined task.

Finally, it should be noted that for the dimensions relevant to the eccentric system described above, the illuminated volume element amount to about 10^3 cm^3. Accordingly, for the case where ρ-values $<10^{-3}$ cm^{-3} the system may then operate as a single particle counter. In this case, a more complex data acquisition, reduction and analysis procedure will require formulation and application. In this manner, however, it would then become possible to establish very low upper limit values for the particle concentrations surrounding the space vehicle.

4.2 LASER PROBING OF COMETARY PHOTO-DISSOCIATION

4.2.1 Cometary Background

4.2.1.1 Motivation and review

In the field of cometary physics, one of the most significant and interesting problems is the determination of the physical mechanism or mechanisms responsible for the production of the observed radicals and ions. To date, convincing evidence exists supporting a resonance-fluorescence mechanism by solar radiation for most of the comet observed molecular and atomic emission. The problems of the mechanisms of dissociation and ionization of most of the stable parent molecules and product fragments remain essentially unresolved.

In spite of a host of attempts to theoretically or experimentally ascribe these phenomena to orthodox theories of simple interactions between the molecules of the cometary atmosphere and the solar

corpuscular or electromagnetic fields only moderate progress has been achieved. Most of these attempts fail by orders of magnitude to produce sufficient material quickly enough to be responsible for the cometary observations.

It is in this area of mechanisms that it may be possible to gain some insight with the proposed gaseous releases. To simply reproduce cometary observations without improving the understanding of the cometary phenomenon, especially with regard to solar interactions, achieves very little other than from a purely spectroscopic point of interest that could probably be better performed in a laboratory. In this report, this experimental aspect is emphasized, from which the observations will enable one to gain insight pertaining to the physical and chemical mechanisms controlling the cometary environment.

Since resonance fluorescence is now believed to represent the fundamental mechanism in exciting the emissions observed in cometary atmospheres, primary emphasis will be given to the mechanisms of dissociation and ionization. However, by no means does this imply that the emission processes should not be studied. It is important to reaffirm the mechanism, especially in the case of an artificial simulation, for several reasons. Firstly, it is important that the effectiveness of the mechanism is quantitatively confirmed. Secondly, it will increase (or decrease) confidence in the validity of cometary simulation, and finally it will permit an extro-atmospheric study of the mechanism over an extended spectral range. Verification by the Swings effect, quantitative intensity distributions or polarization effects will be very important but is not analyzed herein.

It must be remembered that resonance fluorescence has not been successful to date in explaining the OI emissions while the success in explaining the emissions from the cometary triatomics C_3, CO_2^+ and NH_2 has been somewhat meager, emphasizing the need for continued work and observations in this area. Present understanding of the cometary dissociation and ionization processes is poor. If the Whipple proposed frozen iceberg nucleus model is even approximately valid, then

the observed radicals and ions are most likely created by fragmentation of larger stable neutral molecules originating from this nucleus. Somehow, these molecules have to be dissociated and ionized.

In the list of possible cometary parent molecules, N_2H_4 represents the species which will dissociate in the minimum time to form NH_2 consistent with cometary observations. For ionization mechanisms, the orthodox effects of proton collision charge exchange and photoionization are seemingly even further removed from being able to explain the observations. The presumed solar fluxes, molecular densities are far too low to be sufficiently effective.

It is apparent that more work should be performed in this field. It is apparent that there presently exists a both poor understanding of cometary phenomena as well as the solar interaction with an atmosphere. An improvement in this understanding of the cometary phenomena would then be of assistance in the current conception of the Earth's atmosphere.

The radicals observed in the coma are probably products of dissociation processes which occurred following the liberation of parent particles from the nucleus. For instance, the photodissociation of parent compounds such as ABC may be a characteristic process in the coma while only AB radicals radiate in the detectable spectral region.

However, the formation of the molecules observed in cometary atmospheres remains an unsolved problem. According to the results of observations, the decomposition of possible precursors of such typical neutral molecules as CN and C_2 in the solar radiation field is relatively fast.

The characteristic lieftime of parent particles in comets is probably no longer than 10^4 seconds, at unit solar distance. Most present estimates of molecular lifetime are predicated both on the observed distribution of emission intensity in the cometary head and on the assumption of a particular kinematic behavior of the material in the cometary atmospheres.

Even if the methods employed for determining the characteristic decomposition times of hypothetical parent particles are not sufficiently accurate, it seems evident that such processes in cometary atmospheres are relatively fast and require only of the order of a few hours. This is at variance with computed lifetimes obtained for some suggested parent molecules.

Results on prospective parent molecules for cometary radicals (Table 4.1) show that the value of τ_p computed from the photodissociation cross-sections and intensity of solar radiation at frequencies corresponding to the dissociation continuum, is at least 5 to 10 times longer than τ_p obtained from cometary observations. For example, an experimental cross-section for the photodissociation of an unsaturated acetylene molecule C_2H_2, which is one of the suspected parent molecules for C_2, and the solar flux integrated over the dissociation continuum, lead to a lifetime of about 50 hours. Several other relevant compounds such as C_2N_2 which is assumed to be dissociated into CN have lifetimes of nearly 100 hours. C_2H_4, which could be a parent of C_2 with decay time of 4-6 hours produced no C_2 Swan bands (typical of comets) when photodissociated in the laboratory.

These results imply that the probability of dissociation in a cometary atmosphere is orders of magnitude higher than determined from the data available on photodissociation cross-sections and solar radiation flux. The photodissociation process obviously is dominant for the decomposition of the observed radicals, but does not seem to be efficient enough for the dissociation of parent molecules. The lifetimes determined for some components that could be considered as possible parent molecules are $\tau_p = 10^{5.5} - 10^{6.5}$ seconds. By contrast, observations of the CN and C_2 intensity distribution suggest a τ_p value of about 10^4 seconds. The same probably holds for H_2O as follows from the analysis of ultraviolet observations of neutral hydrogen and OH[32].

The differences are so striking as to cast doubt on the mechanism of position in the production of the observed neutral molecules in comets so that other theories have been proposed.

TABLE 4.1

SPACE LIFETIMES FOR VARIOUS POSSIBLE PARENT COMPOUNDS

Molecule	Lifetime (hr)	Radical Yielded
$HC \equiv C - CN$	$\geq$18 (to 1850Å)	CN
$CN - C \equiv C - CN$	$\geq$29 (to 1850Å)	CN
C_2N_2	344.7 (to 1850Å)	CN
	84.7 (to 1550Å)	
	58.8 (to 1350Å)	
CH_2CN	$\geq$3342 (to 1850Å)	CN
	$\geq$944 (to 1500Å)	
	$\geq$719.4 (to 1300Å)	
CH_4	>28 (to 980Å ioniz.)	CH
$H_2C \equiv CH_2$	>23.0 (to 1850Å)	C_2
	>8.3 (to 1500Å)	
	>4.3 (to 1050Å ioniz.)	
HC CH	>117.9 (to 1850Å)	C_2
	>47.8 (to 1500Å)	
	>43.0 (to 1000Å ioniz.)	
N_2H_4	0.75 (to 1850Å)	NH_2
	0.70 (to 1500Å)	
	0.70 (to 1400Å)	
CH_3NH_2	$\geq$0.95 (to 1850Å)	NH_2
	$\geq$0.91 (to 1500Å)	
	$\geq$0.90 (to 1850Å)	
NH_3	5.0 (to 1850Å)	NH_2
	4.3 (to 1500Å)	
	4.1 (to 1050Å ioniz.)	
H_2O_2	1.6 (to 1850Å)	OH
H_2O	81.2 (to 1850Å)	OH
	22.7 (to 1500Å)	
	20.2 (to 1000Å ioniz.)	

Consequently, a specifically designed cometary release program to measure photodissociation rates of cometary molecules is of high value.

4.2.2 Advantage of Laser Probing of Photo-Dissociation

The relatively simple but important rationalization for the proposed laser fluorescence solar photo-dissociation experiment is that photo-dissociation constants are long, sometimes many hours (see Table 4.1), and the amount of cometary materials released may be too small to provide an observable signal due to solar fluorescence. The laser allows one to perform measurements on daughter species owing to its output power delivered on a line (atomic or molecular) which can be many orders of magnitude greater than that provided by the sun. For example, for $\Delta\lambda = 0.1$ angstroms at 5720 Å the solar flux is approximately 10^{13} photons/cm^2 sec (or 1 microjoule). Current dye laser systems offer pulsed and CW sources in this spectral region as shown in Table 4.2. Typical are a CW tunable laser, using an Argon laser to pump Rhodamine dye yielding approximately 0.1 watt between 5650 to 6450 Angstroms, and a dye laser system (from 4350 to 7000 Å for various dyes) giving powers of the order of a megowatt for pulse widths of the order of a microsecond, and repetition rates of the order of 1 to 5 per second.

Consequently, it can be seen that, depending on the specifics of the molecule under examination after photo-dissociation, fluorescence of the daughter fragment can be readily examined with an appropriate laser as contrasted to passive observations of solar fluorescence. Reference is made to a recent study by Baardsden and Terhune (31) in which a dye laser at the frequency of 2880 Å was utilized to measure concentration of the hydroxyl radical at levels of 10^6 to 10^8 cm^{-3}.

4.2.3 Preliminary Mathematical Analysis

The preliminary mathematical analysis of the experiment is applied below. It is assumed that the released molecular density is

TABLE 4.2

	Laser-Pumped Pulsed Dye Laser	Flash Lamp-Pumped Pulsed Dye Laser	CW Dye Laser
Peak Power	10^7 W (Giant Pulse) 10^8 W (Mode-Locked)	Several MW	~2 W
Energy per Pulse	Up to Several Joules	Up to Several Joules	_____
Pulse Duration	5 ns to 30 ns	50 ns to 1 ms	_____
Mode-Locked Pulse Duration		10 picosec.	1.5 picosec.
Tuning Range	340 nm to 1200 nm (All Dyes) 375 nm to 550 nm (One Dye)	340 nm to 700nm	525 nm to 710 nm
Linewidth	40 MHZ (0.00005 nm) Tuned 10 nm Untuned	40 MHZ (0.00005nm) Tuned 5 nm Untuned	~10 MHZ (0.00001 nm) ~30 nm Untuned
Efficiency	$\frac{\text{Optical Output}}{\text{Optical Input}}$ ~0.5	$\frac{\text{Optical Output}}{\text{Electrical Input}}$ ~10-2	$\frac{\text{Optical Output}}{\text{Optical Input}}$ ~0.35

such that collision can be ignored and that the trajectory is straight and ambient collision is also negligible.

The density, n in a spherical shell of thickness, dx at a radial distance, x from a spacecraft of radius, R is given by

$$n = \frac{N_x}{V} (dt) = \frac{N_x}{V} \frac{dx}{u} \tag{4.5}$$

where N_x is the number of molecules per unit time entering the shell at x, dt is the time required to traverse the distance, dx at velocity, u and $V = 4\pi (R + x)^2 dx$ is the approximate volume of the shell. Consequently,

$$n = \frac{N_D}{4\pi (R + x)^2 u} \tag{4.6}$$

Assuming a photo-dissociation lifetime τ, the number of molecules photo-dissociated at time, t is n_d, where

$$n_d = n \left[1 - \exp - \left(\frac{t}{\tau}\right) \right] \quad \text{or} \tag{4.7a}$$

$$n_d = n \frac{t}{\tau} \quad \text{for} \quad t \ll \tau \tag{4.7b}$$

and for

$$t = \frac{x}{u}$$

$$n_d = \frac{N_D x}{4\pi (R + x)^2 u^2 \tau} \quad \text{or} \tag{4.8}$$

$$n_d = \frac{N_D}{4\pi x u^2 \tau} \quad \text{for } R \ll x \tag{4.9}$$

As a modification when collision with the ambient is important:

$$n_d = \frac{N_D \exp - (x/\lambda)}{4\pi \; x \; u^2 \; \tau} \tag{4.10}$$

where λ is the mean free path and there is an exponential survival relationship. In addition, should the release be non-isotropic but controlled into a solid angle, Ω then

$$n_d = \frac{N_D \exp - (x/\lambda)}{\Omega \; x \; u^2 \; \tau} \qquad \text{or} \tag{4.11}$$

$$n_d = \frac{N_D}{\Omega \; x \; u^2 \tau} \qquad \text{for} \quad x \ll \lambda \tag{4.12}$$

4.2.4 Calculation of Laser Fluorescence

For a unit cross-section path perpendicularly through the middle of the effused gas, the path length intersected is approximately

$$\ell = 2x \tan \theta \tag{4.13}$$

where θ is the conical half-angle and similarly the solid angle is given by

$$\Omega = 2\pi \; (1 - \cos \theta) \tag{4.14}$$

The total number of photo-dissociated molecules in the cross-section per cm^2 then is approximately given by

$$n_t = \ell \; n_D \tag{4.15}$$

and utilizing Equation (4.12)

$$n_t = \frac{\tan\theta}{\pi\,(1-\cos\theta)} \quad \frac{N_D}{u^2\,\tau} \tag{4.16}$$

For a molecular absorption cross-section, σ_p, I_p photons per pulse, and a receiver area A, the photons received per pulse are

$$n_p = \frac{I_p\,A\sigma}{4\pi\,x^2}\;n_t \tag{4.17}$$

$$= \left(\frac{I_p\,A\sigma}{4\pi\,x^2}\right)\left(\frac{\tan\theta}{\pi\,(1-\cos\theta)}\right)\left(\frac{N_D}{u^2\,\tau}\right)$$

Selecting reasonable values:

N_D	= 10^{24}	molecules/second	σ	= 10^{-19}	cm^2
A	= 10^3	cm^2	I_p	= 10^{17}	photons/pulse
τ	= 10^4	second (several hours)	x	= 10^3	cms (10 meters)
u	= 10^4	cm/second	θ	= 10^0	

we obtain

$$n_p = 3 \times 10^6 \text{ photons/pulse}$$

Previous considerations herein have indicated that with proper design for gating, crossing of the illuminated effused beam with field-of-view of the detector, and use of spectral filters, laser molecular resonance scattering has significant advantage over direct solar scattering.

Specific engineering design will not be undertaken here as in the particle case since it has been the purpose here only to demonstrate the feasibility and advantage of the scheme for determining the photo-dissociation constants of cometary species.

5.0 FUTURE WORK

It is recommended that a specific experiment design study be performed for a combined laser probe involving particulates, effluxed gases, and cometary materials. A dye-laser system may be employed along with a single detection probe so that favorable cost effectiveness can be achieved as well as reduced experimental complexity.

The major remaining design problem is that of defining appropriate release mechanisms and experimental integration. In this study, the behavior of the gaseous and particulate clouds is established on the basis of a single parameter. What is now required is a more detailed analysis to establish both cloud shape and dynamics which takes into account the variation of molecular mass as well as the phase functions associated with particulate scattering.

APPENDIX A

APOLLO SPACECRAFT CONTAMINATION RATES

Gas leaks in the cabin of Apollo are expected to be at a rate

$$\frac{dm}{dt} \simeq 100 \text{ gm/hr} = 2.8 \times 10^{-2} \text{ gm/sec.}$$

Of this material a large fraction is cabin gas, an unknown portion is particulate debris, and up to 1% by mass is water vapor. Assuming that the process of escaping through porosities of the spacecraft cools the gas sufficiently so that all the water vapor crystalizes, a continuous ejection of

$$\frac{dm}{dt} \sim 3 \times 10^{-4} \text{ gm/sec}$$

of particulate ice results. An analysis of the thermodynamics of such escape (Fulk, 1967) suggests that only a negligible (but unknown) fraction crystalizes.

Water produced by fuel cells and liquid human wastes are stored in a tank with a capacity of approximately 1.7×10^4 gm with the expectation that the reservior must be dumped every 12 hours. It is assumed that this material is expelled by the cabin pressure at a velocity $u_o \sim 7 \times 10^2$ cm/sec and that initial evaporation cools the water sufficiently that a major portion forms either snow or droplets of ice.

The periodic operation of orientation jets expells material at a rather high velocity. Although the ejecta from dry nitrogen jets can be expected to sublime immediately, hypergolic reaction engines produce large quantities of water which, presumably, crystalize rapidly. For example, when the Apollo system is employed for astronomical observation it desperses.

$$\Delta m \sim 2 \times 10^2 \text{ gm}$$

of material in brief bursts every 20 minutes.

The rate of outgassing of material from a spacecraft is extremely difficult to evaluate. Even properly prepared paints appear to evaporate at a rate of $\sim 10^{-10}$ gm/cm^2/sec which would lead to

$$\frac{dm}{dt} \sim 10^{-4} \text{ gm/sec}$$

for a satellite with an area of 10^6 cm^2. Manned spacecraft are equipped with ablation shields of porous ceramic material whose outgassing properties are also unknown.

APPENDIX B

LASER TRANSMITTER AND RECEIVER DESCRIPTIONS

In this appendix an available laser transmitter is described which is suitable for the proposed particulate experiment. Much of the information is based upon present state of the art information available from a variety of published sources.

The function of the proposed laser transmitter is to generate radiation output at 6943Å. This is accomplished by the use of a laser resonator employing a ruby crystal as an active lasing medium. The radiation emanates from a single aperture located at the exit window of the laser transmitter.

A. LASER TRANSMITTER SYSTEM

The proposed Laser Transmitter assembly is designed to have the following characteristic features:

(a) Output Energy 6943Å >100 mj

(b) Q-switched Pulse Length -< 100ns, typically 30 ns

(c) Cooling - Deionized flowing water

(d) Pulse Repetition Rate - 1 pps

(e) Q-switch - Rotating Prism Reflector

(f) Size - 3.75" x 6.25" x 17.00"

(g) Weight - 17 lbs. maximum (exclusive of cooling system, power supply and supporting structure).

The Transmitter Unit will contain the following:

(a) Laser Interferometer

(b) Energy Storage Pulse Forming Network

(c) Control electronics

(d) Low Voltage regulator for timing logic circuit

(e) Connectors for battery power input, Hi Voltage Power Supply input and Laser start pulse output

(f) Laser Cooling System

1. Laser Interferometer

The Laser Interferometer will consist of a close coupled double compartment cavity containing a 6 mm x 3" high quality ruby rod and an FX38A E.G.G. Flash Lamp separated by UV filter glass. The separate coolant flow paths for the flash lamp and rod will reduce the temperature gradient along the ruby rod resulting from the transverse flow of liquid coolant. The interferometer will be approximately 12" long and will be terminated on one end by a rotating prism Q-switch driven at 24,000 rpm by a D.C. motor and at the output end by a resonant type partial reflector.

a. Q-Switch

The Q-switch is the optical device used to control the optical feedback in the laser. The laser interferometer optical path has the basic elements of the laser rod, a semitransparent output reflector (resonant reflector) on one end, and a totally reflective Porro prism on the other end. A rotating prism in the Q-switch allows the two end

reflectors to become optically parallel for an instant of time. It is at this instant that photons emitted from the laser rod are reflected back and forth between the reflectors stimulating other active atoms in the rod to emit their energy and the emission of an intense and narrow light beam through the resonant reflector.

A magnetic slug on the Q-switch rotor passes by a magnetic pickup coil on the Q-switch housing once during each revolution of the rotor. This coil, which is wound on a permanent magnet, is connected to the input of the magnetic pickup amplifier. When the slug passes the coil winding, it cuts across the magnetic field and induces a voltage pulse in the pickup coil. The pulse from the magnetic pickup coil is passed to a magnetic amplifier and a time coincidence circuit. This circuit gates and delays the magnetic pulse output from the amplifier so that initiation of the flash lamp operation occurs at an optimum time relative to laser emission.

b. Lase Start Pulse

An H.P. PIN Photodiode will be mounted such that its sensitive area is facing the apex of the fixed porro prism in the Q-switch It will be connected in a circuit such that at the time of lasing a 4 volt negative going pulse (+4 to 0) will be generated. This signal will be present at a coaxial connector on the front panel of the transmitter unit.

1. Transmitter Electronics

The electronic transmitter sub-system involves state of the art capability. For reference a brief description of the various

elements of this system follows.

a. Control Circuit

The control circuit board is a plug-in printed wiring assembly which contains circuits providing the following functions.

(a) Enables the charging of the Pulse Forming Network capacitors.

(b) Senses the high voltage charge on the Pulse Forming Network and removes the charge enable signal when the proper charge level is attained.

(c) Processes the magnetic pickup signal from the Q-switch motor through an adjustable delay circuit to produce a Krytron trigger signal which fires the flash lamp at the optimum time prior to lasing.

(d) Produces a "ready to fire" signal at a one pulse per second rate to control the repetition rate.

b. Triggering Circuit

Triggering of the flash lamp is initiated by the KRYTRON TRIGGER signal from the control board. This trigger is transformer coupled to the grid of the Kyrtron tube which acts as a high voltage switch. The Krytron tube generates a fast 2000 volt pulse which is fed to the primary of the trigger transformer. The secondary of the trigger transformer is in series with the flash lamp and forms part of the lamp discharge circuit. The high voltage pulse (12 KV) generated in the secondary of the trigger transformer causes ionization of the flash lamp and the discharge of the PFN capacitors.

B. HIGH VOLTAGE POWER SUPPLY UNIT

The Power Supply Unit is designed to operate with the Laser Transmitter Unit to charge the Pulse Forming Network 80 μfd energy storate capacity during the one second interim between firings.

The characteristics of this unit are as follows:

(a) Input Voltage - 20-30 VDC

(b) Input Current - 10 amp peak max at 25V while charging

(c) Size - 6.5" x 8.5" x 6"

(d) Weight - 8 lbs.

1. Operation

The function of the High Voltage Power Supply is to, upon receipt of the CHARGE ENABLE signal from the control board, charge the pulse forming network capacitors to the required level.

It contains an oscillator circuit the frequency of which is decreased as pulse forming network charge voltage increases.

An impedance matching network in conjunction with the load (PFN energy storage capacitors) reflects an approximately stable load to the source during the charging cycle as a result of the decreasing oscillator frequency. This stabilization of the effective load impedance increases power supply efficiency.

C. POWER REQUIREMENTS

The input power requirements for the sub-system are listed below:

(a) <u>High Voltage Power Supply</u>

The energy stored in the PFN capacitor is:

$$E = \frac{1}{2} CV^2$$

where

C = PFN capacitor value

V = charge voltage

Typical values for this system are:

C = 80 microfarads

V = 1600 volts

so that $E = \frac{1}{2} (80 \times 10^{-6}) 1600^2$ joules = 102.4 joules

A typical power conversion efficiency is 75%

Input energy = 136.5 joules

Since the charge time is one second

Input power = $\frac{\text{input energy}}{\text{time}}$

(b) <u>Control Circuit Board</u>

5 volts at .4 amps = 2 watts

(c) <u>Q-Switch Motor</u>

24 volts at .5 amp = 12 watts

Total input power requirement is therefore 150.5 watts.

$$\text{Input current} = \frac{\text{input power}}{\text{input voltage}}$$

$$= \frac{150.5 \text{ watts}}{24 \text{ watts}}$$

$$= 6.3 \text{ amps}$$

D. LASER COOLING

The cooling of the laser cavity is essential to prevent excessive heating of the ruby rod and hence, a deterioration of the transmitted pulse. In order to maintain the ruby rod at a temperature of 25 $\pm$ 5°C, one can consider both closed and open ended techniques using coolant water at both room temperature and at reduced temperatures. Preliminary calculations indicate that savings in water flow rates (and hence total weight of water required), by as much as a factor of two to three can be realized by operating with reduced water inlet temperatures. Present estimates of total water required for a four-minute operating period range from two to six gallons(or 15 - 45 lbs) with the lower value applying to an inlet temperature of about 4°C. Depending upon the available weight budget, it may become necessary to take advantage of this factor, recognizing, of course, that in this event certain inconveniences may be encountered. More detailed calculations are required to identify and assess the various trade-off factors involved.

The actual water flow through the laser cavity may be accomplished by a systolic pump or by a pressurized system. The former method offers the unique advantage of not introducing any contaminants into the water system since the water is forced through the cavity by sequentially squeezing a hose and moving the coolant through the cavity.

E. RECEIVER SYSTEM

The receiver consists of a collector mirror, a system of baffles,

a light guide, a cylindrical lens, an interference filter, and a PM tube with associated electronics.

The collector mirror is part of a 40" radius sphere and its edge is of an elliptical configuration (14.25" x 16.00") so that the required collector area is shielded when projected on to the mirror from the off-axis direction. The mirror consists of an electro-plated nickel substrate which is attached to a torus with structural adhesive. The torus is kinematically mounted to a deck plate.

The entire image plane assembly can be installed on one rigid baseplate, which is in turn mounted on two deck plates. The light guide consists of two appropriately shaped aluminum plates which are provided with a Kanengime coat on one side (the inside) and polished and two highly polished sheetmetal strips which are attached to the contoured sides of the shaped plates to constitute the light guide. The receiver electronics are not considered herein since their design would necessarily be dependent on th final experimental configuration and data handling require ments. Finally, it has been estimated that the total payload weight involved is approximately 200 lbs.

REFERENCES

1. Pressman, J., Final Report NASw-1745, GCA Corp., 1970.

2. Ney, E. P. and W. F. Huch, Science, 153, 297, 1966.

3. Baurer, T., Final Report, POWO No. 71 F022, GE. Philadelphia, Pa.

4. Kovar, N. S., Sky and Telescope, 152, March, 1968.

5. Grenda, R. et al, Space Research IX, North Holland Publishing Co., Amsterdam, 1969.

6. Hoffman, J. H. et al, Proc. Third Lunar Science Conf., Houston, January, 1972.

7. Buffalano, C., Bellcomm. Inc Memo, April 19, 1968, subject: The Spacecraft Debris Cloud and Optical Environment.

8. Newkirk, G. N. Jr., PASS 15, 1267, 1967.

9. Ball Brothers Research Copr., 1967, ATM Contamination Study (Contract NASw-1386).

10. Alyea, F. N., G.E. Memo, Philadelphia, 1967.

11. Pikus, L., G.E. Memo, Philadelphia, 1967.

12. Silverman, S. M. and Lloyd J.N.F., Science, 157, 917, 1967.

13. Wolff, C., Science, 158, 1045, 1967.

14. Kovar, N. S., et al, PASS, 17, 1967, 143-154.

15. Buffalano, C., J. Geophys. Res., 76, 1, 1971.

16. Sharma, R. D. and C. Buffalano, J. Geophys. Res., 76, 1, 1971.

17. Scialdone, J. J., NASA TN D-6682, May 1972.

18. Scialdone, J. J., NASA TN D-6645, May 1972.

19. Wallace, D. A. and R. L. Chuan, Celesco 113, May 166, Celestial Research Corp., S. Pasadena, Calif.

20. Klingman, E. E., IES/AIAA/ASTM 6th Space Simulation Conference, May 1-3, 1972, New York, N.Y.

21. Jashbar, P. W., ibid.

22. Kurtz, R. I. and J. R. Williams, ibid.

23. Greyerbiehl, J.M., ibid.

24. Dewey, R. L., ibid.

25. Visentene, J. T. et al, ibid.

26. Stephens, J. B. and Wallace, D. A., Proc. of AIAA Space Simulation Testing Conference, AIAA Pub. CP-11, November, 1964.

27. Penndorf, R., "Tables of Mie Scattering Functions for Spherical Particles, "Geophysical Research Paper No. 35.

28. Penman, H. H., Heller, W. and Pangonis, W.J., Angular Scattering Functions for Spheres, Wayne State Univ. Press, Detroit, Mich., 1966.

29. Van de Hulst, H.C., "Light Scattering by Small Particles," John Wiley and Sons, Loneon, 1957.

30. Snarely, B.B., "Organic Dye Lasers: Headed Toward Materity", Electrosticol System Design, April, 1973, 30.

31. Baardsden, E. L. and R. W. Terhune, Detection of OH in the atmosphere using a Dye Laser, abstract B10 in 1972 quantom Electronic Conference (VII th).

32. Keller, H. U., Mitl asts. ges. homb. No. 30, 143, 1971.